SAND2019-9816B

Quantitative multiscale microscopy of defects and deformation for application to materials modeling

Hojun Lim[1], Jay D. Carroll[1], Douglas L. Medlin[2] and Khalid Hattar[1]

[1]Sandia National Laboratories, Albuquerque, NM 87185, USA

[2]Sandia National Laboratories, Livermore, CA 94550, USA

Contents

1. Introduction

Big data generated and processed from recent state-of-the-art imaging techniques are often utilized in computational modeling and analysis. With the explosive progress in computing resources, computational materials modeling for guiding materials design has become an important topic in the materials research and engineering communities. Development of these multiscale computational tools and high-resolution characterization techniques is regarded as one of the most significant transformational trends of the last 25 years in metal plasticity [1]. Furthermore, recent high-performance computing (HPC) combined with computationally expensive, high-fidelity computational materials models informed from high resolution imaging techniques has become a viable option to model various phenomena in large materials systems. However, as pointed out by Kalinin [2], two major issues in using big data in imaging techniques and computational modeling are (1) a need for closer coupling of experiments and simulations to improve the fidelity of the model and (2) disparity in the length scale between atomic scale experiments and engineering scale modeling techniques.

Figure 1 shows representative examples of different computational tools and imaging techniques used in materials design from atomic to structural scales. These various computational and imaging methods are used to characterize crystalline structural defects across the wide range of time and length scales. For example, structural defects and microstructural features are considered from individual vacancies and solute atoms (atomistics), dislocation line segments (dislocation dynamics) and grain-level heterogeneities (polycrystal plasticity). Computational models directly or indirectly use the data generated from imaging techniques as an input (initial configuration) or validation (final configuration) to investigate statistical distributions and evolutions of defects.

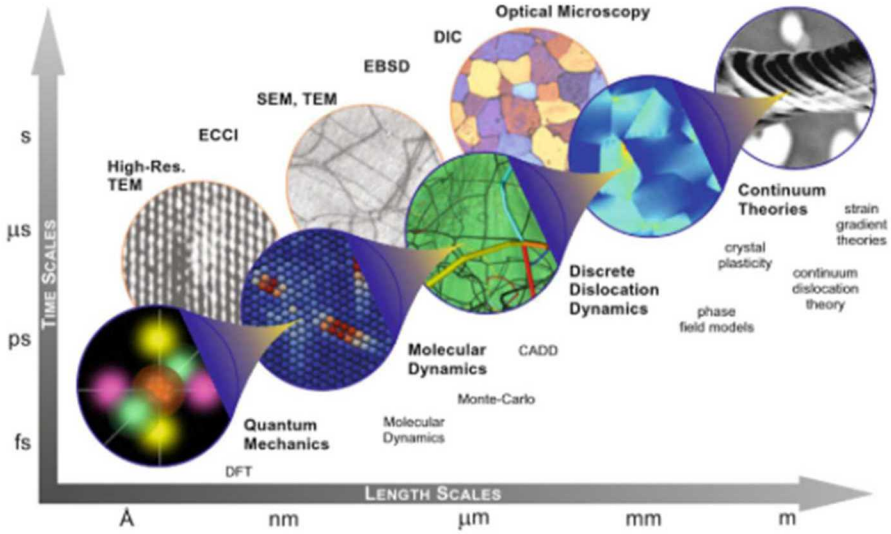

Figure 1. Computational methods and imaging techniques in various time and length scales. From reference [3].

For example, computational quantum mechanical modeling methods, e.g., density functional theory (DFT), are widely used to investigate the electronic structures using functionals of electron density. The results of such simulations are often compared with microscopy data to understand structural and chemical properties of interfaces in thin films [4, 5] or surface structures of atoms and nanoparticles [6-8]. At the atomic/molecular level (10^{-9} – 10^{-7} m), molecular dynamics (MD) is widely used to understand the physical movement and relaxations of individual atoms and molecules from the potential energy of the system and the forces on all the atoms. MD simulations are suitable for the study of defects at the nanoscale and to directly compare with high resolution Transmission Electron Microscopy (TEM) images, i.e. morphology and intrinsic structures in nanofibers [9], grain boundaries and twin boundaries [10], deformation mechanisms [11], irradiation damage [12], strain/slip transfer at interfaces [13] and fracture and failure [14, 15]. Discrete dislocation dynamics (DDD) techniques explicitly model dislocation lines as an elastic inclusion embedded in an elastic medium. Dislocation dynamics are directly compared with TEM and SEM measurements to compare evolution of dislocation densities [16] and dislocation substructures [17]. Meso-scale or grain-scale plasticity models consider aggregate behaviors of defects in continuum framework (10^{-3} – 10^{-1} m).

Recent grain-scale plasticity models consider microstructural features, such as grain sizes and shapes as well as crystal structures and orientations, and their defect densities are either explicitly modeled (i.e. voids and precipitates) or treated as evolving internal state variables (i.e. dislocation densities). Volume-averaged defect densities can be directly compared with various electron and optic-based microscopy techniques in realistic length and time scales.

This direct use of big data generated from high resolution imaging techniques and computational models outlined above is beneficial to both fields and enabled further advancements. In the following sections, we review recent advances in electron microscopy techniques used to characterize crystalline structural defects and discuss the use of big data in imaging and characterization techniques. Also, we discuss the coupling of microscopy and modeling techniques and the limitations and future directions using the big data to advance fundamental materials understanding.

2. Atomic resolution imaging of defects

Tremendous advances in instrumentation and methods for atomic-resolution Transmission Electron Microscopy (TEM) over the past three decades have broadly expanded the possibilities for investigators to directly interrogate the atomic-scale structure and composition of crystal defects. Increasingly these analyses are moving beyond simple, qualitative images of atomically resolved structures and more toward quantitative structural and chemical measurements of atomic columns that can be directly related to and compared against theoretical predictions. Important information regarding crystal defects drawing on atomically resolved information include the structure and composition at the defect core, the arrangement and topological character of defect arrays, and the near and intermediate scale strain field distribution.

Atomic resolution techniques for investigating crystal defects include high resolution transmission electron microscopy (HRTEM or HREM) and high-resolution scanning transmission electron microscopy (HRSTEM). These microscopies have been greatly

advanced by the development of aberration correctors for the electron lenses [18-21], enabling sub-Ångstrom spatial resolution and improved image contrast. In HRTEM, a relatively large area of the specimen (~100 nm^2) is illuminated simultaneously by the nominally columnar electron beam. The electron wave function exiting the specimen is focused using the objective lens, and the image is collected on an area detector. Conversely, in HRSTEM, a highly convergent electron beam, focused by the condenser lens, is rastered across the specimen and the signals from the electron interactions with the specimen are collected in series, pixel-by-pixel, on various detectors. For instance, in high angle annular dark field (HAADF) STEM imaging, an annular detector is used to collect electrons scattered to high angles beyond the low-order Bragg reflections. Since the signal in this angular regime depends strongly on atomic number, the technique provides not only atomic resolution but also compositional sensitivity. A wide variety of other signals can also be detected in STEM imaging. For instance, annular bright field (ABF) imaging provides good sensitivity for light elements [22], such as oxygen and nitrogen, providing complementary information to the high atomic number information that is more readily obtained via HAADF-STEM. The emergence of multi-channel, segmented STEM detectors [23, 24] and fast and robust pixelated electron detectors [25, 26] is allowing for increasingly sophisticated treatments of the angularly resolved scattered electron distribution, to the level of collecting and analyzing full diffraction patterns for each pixel of the real-space image. Furthermore, by coupling the scan signal to spectroscopic detectors, such as an electron energy loss spectrometer (EELS) or, increasingly, a large area energy dispersive x-ray spectrometers (EDS), atomically resolved compositional and electronic structure information can be obtained to complement the structural imaging providing great insight into the structure and chemistry vicinal to defects and interfaces. Finally, the emergence of atomically resolved electron tomography techniques [27] are opening up the possibility of extending crystal defect analyses from two-dimensional projections to more complex, three-dimensional configurations.

In this section, we provide an overview of atomic resolution electron microscopy applied to the analysis of crystal defects. Our emphasis is not on the imaging physics, as this

topic is well addressed elsewhere (e.g. [28-30]). Rather, our intent is to outline some of the important data handling and analysis aspects of atomic resolution defect imaging. As we will see, the requirements for accurate quantification and the demands for acquiring and analyzing the large data sets, which are often multi-dimensional, is motivating growing application of data science both to the data analysis as well as to understanding how best to optimize the data acquisition itself.

2.1 Data acquisition

In order to ensure high fidelity and accuracy in the subsequent analysis of atomic resolution images of crystal defects, it is critical that imaging artifacts be accounted for and, ideally, corrected. For instance, in HRTEM imaging, aberrations in the intermediate and projector lenses can introduce long-range distortions, such as pincushion, barrel, and spiral distortions [31], that can strongly affect the results of strain mapping. Since these distortions can be stable over time, they can be measured and corrected by obtaining a lattice image from a single crystal reference material under identical imaging conditions to the image of interest. Another issue is to ensure that there are no reversals of image contrast with the image region. Such contrast reversals will impact the efficacy and interpretation of any peak finding approaches. Furthermore, in strain measurements using the Geometric Phase Analysis (GPA) method, discussed below, the change of image phase associated with the reversal of contrast will yield an unphysical strain measurement. This is a particular challenge for HRTEM imaging where small variations in local thickness or specimen tilt can lead to contrast reversals. HAADF-STEM techniques are much more robust in this regard, although as we discuss next, STEM techniques present other challenges related to probe and drift stability.

For atomic resolution STEM imaging, two common sources of imaging artifact are instabilities in the positioning of the scanning probe itself and overall drift of the specimen. Conventionally, STEM images are acquired by scanning one row of pixels at a time, then advancing to the next row. Electronic instabilities in returning the probe to the beginning of the row for each sequential scan line can lead to local image distortions known as "fly-back errors", which can be exacerbated at fast scan rates. More generally, local

instabilities in the probe positioning throughout the scan acquisition produce local image registration errors that depend on the directionality with respect to the fast and slow scan directions. One approach to compensate for such local instabilities is simply to collect a series of images which are then aligned and averaged together. Furthermore, if the images are acquired at orthogonal scan rotations, then the asymmetry in the local distortions between the fast and slow scan directions can be cancelled [32].

Reconstruction algorithms to correct for these local instabilities in single images have also been proposed and demonstrated. These approaches draw on the inherent redundancy of oversampled atomic resolution to compare and shift adjacent rows of pixels to minimize phase discontinuities [33], in the case of Fourier-based methods, or to maximize local correlations, in the case of real-space methods [34].

Specimen drift poses a further challenge. Because HRTEM is a parallel acquisition process, specimen drift during image acquisition produces a directional blurring of the image, and so is generally immediately obvious. In contrast, STEM images are acquired serially, with probe dwell times on the order of milliseconds per pixel. Thus, moderate specimen drift results not in blurring, but rather a geometrical distortion of the acquired image. This distortion can be corrected by application of a compensating affine transformation. If the image contains regions of perfect crystal, the affine transformation is that needed to restore the reference regions to the known, undistorted configuration (and can be determined, for instance, by measurement of the observed interplanar angles in comparison to the known crystal structures). In the context of strain mapping, the assumption, of course, is that these reference regions are suitably far from crystallographic defects to be unaffected by their strain fields.

Alternatively, in the absence of this *a priori* crystallographic information, the required correction can be established from a measurement of the direction and rate of the drift [34, 35]. Of particular note, Sang and Le Beau [35] have developed an approach in which a series of images are collected at different scan rotations, over the full range of 0° to 360°. Since the drift distortion is a function of its rate and direction with respect to the

scan direction, the drift parameters can be directly measured from the image series. Moreover, once corrected, the images can be aligned and summed together, improving the signal-to-noise by averaging out shot noise and the random distortions resulting from local probe instabilities.

Finally, the potential for beam induced artifacts, whether by knock-on displacement damage or ionization damage, is always a significant concern at the high electron dose rates typical of atomic resolution imaging. Here, quantitative data analysis methods are also providing benefit. One approach is to acquire a series of low-dose images that can be subsequently registered and analyzed to reveal systematic image changes over time that would be indicative of beam damage [36]. In this way, the optimal tradeoff between signal-to-noise and beam-induced artifacts can be directly assessed. Image registration can be done through standard FFT-based cross-correlation algorithms, although this approach can fail in very noisy images, as is the case for low-dose imaging. More robust image registration approaches, based on non-local means analyses, have been established and applied with success to low-dose atomic-resolution STEM imaging [36]. In addition to challenges with image registration, images acquired with fast scanning can suffer from exacerbated “fly-back errors”. Alternative raster patterns, such as spiral scanning, offer a route to avoid this difficulty [37]. Alternative scan patterns also form the basis for emerging, compressed sensing methodologies for low-dose atomic resolution STEM imaging [38]. In these techniques, a sparse and randomized sampling pattern is used to collect the data, which is then reconstructed using an in-painting algorithm [39-42]. An example from atomic resolution observations of $NiTiO_3$ [40] is shown in Figure 2.

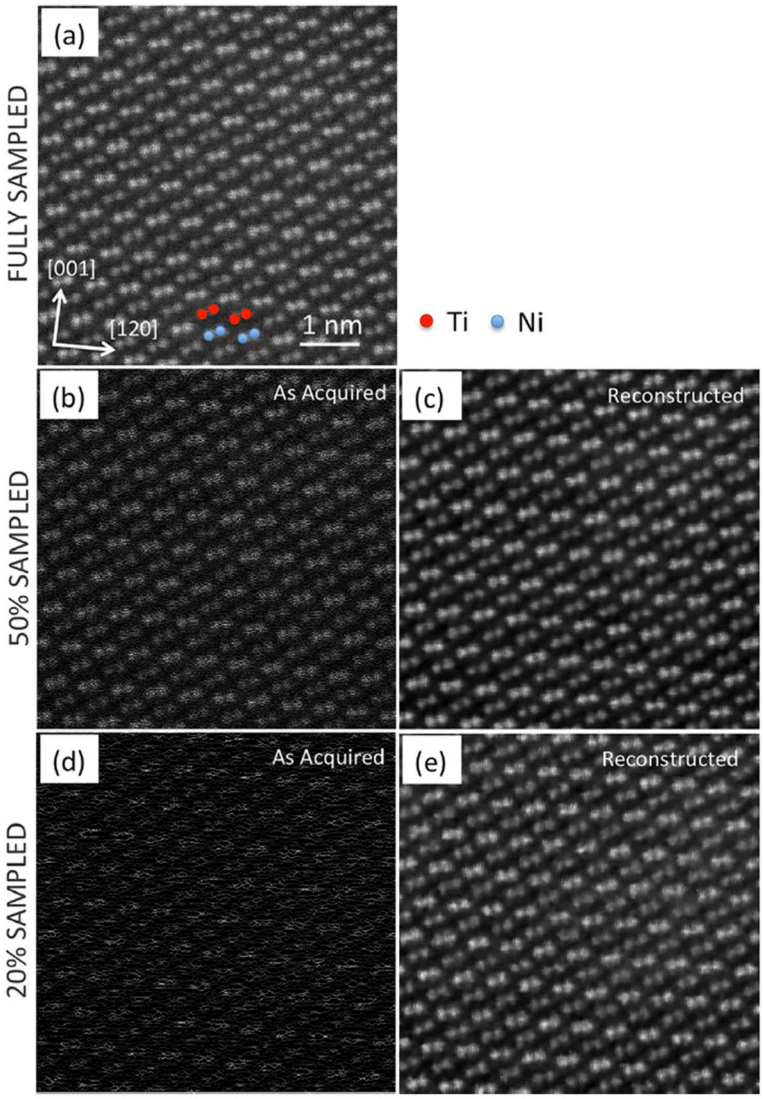

Figure 2. Compressed sensing provides a route to reducing imaging dose for beam sensitive materials. The example here shows atomic-resolution HAADF-STEM images of $NiTiO_3$ acquired with a random sampling pattern at different levels of sparsity (b) and (d) and the corresponding image reconstructions. From reference [40].

2.2 Core Structure of Crystal Defects and Interfaces

Atomic resolution electron microscopy has long played a vital role in advancing our understanding of the atomic configurations at the cores of crystal defects and interfaces. Such observations have been particularly impactful when made in conjunction with theory

and modeling efforts. For instance, experimental measurements of grain boundary structures have provided important test cases for validating the efficacy of different atomistic modeling approaches [43-48]. An example showing a comparison between atomistic models and peak positions from HAADF-STEM images for two grain boundaries in Fe is shown in Figure 3. They have also helped to challenge and advance our current theoretical frameworks for interpreting grain boundary structure [49-54], our notions of interfacial line defects and their relaxations [55-58], and our fundamental knowledge concerning the structure and relaxation of grain boundary junctions [48, 59].

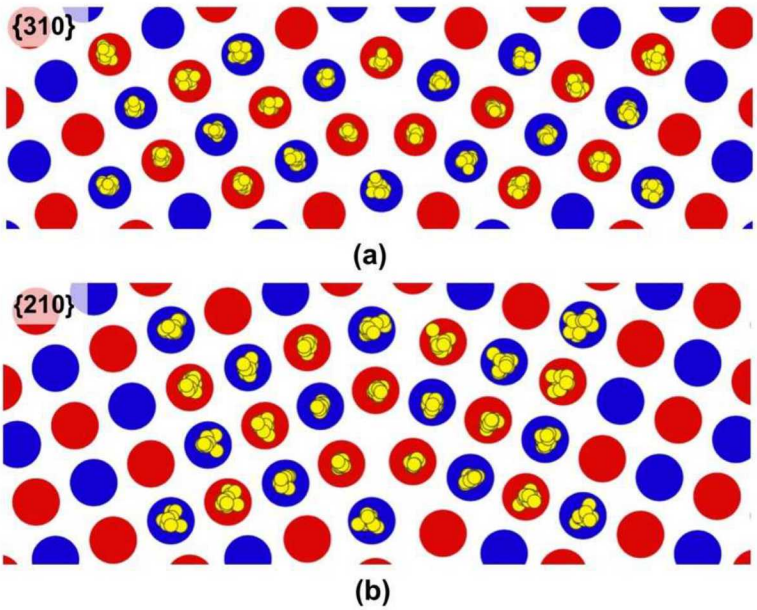

Figure 3. Atomic resolution microscopy techniques can be used to validate the predictions of atomistic modeling. Here, the predictions of atomistic simulations for the Σ=5 {310} (a) and Σ=5 {210} (b) grain boundary in Fe (red and blue), computed using the Mendelev potential [60], are compared with intensity peak positions (yellow) observed by HAADF-STEM in an experimental grain boundary. From reference [48].

The most basic level of comparison between experimentally observed and modeled structures is often to relate the positions of the intensity peaks (or minima) to the predicted atomic positions for the defect. The simplest approach to determine the peak positions is to search for local maxima in the image. However, to improve robustness with respect to noise, the starting image is typically pre-processed. Approaches to pre-processing for

peak finding include simple real-space smoothing operations (such as median filtering or Gaussian smoothing), Fourier filtering to suppress high spatial frequency components [61], and Wiener filtering [62, 63]. Another approach is to cross-correlate a template function (e.g., of an atomically resolved peak or structural motif) and then perform a search for the maxima in the cross-correlation function [64, 65]. Following this initial determination of the peak positions, approaches to improving the peak localization include filtering to eliminate superfluous peaks within an exclusion radius, performing a local intensity of mass refinement [66, 67], or fitting the local signal to a model for the peak (such as a Gaussian function) [32].

Although this approach serves as good first cut at determining the atomic structure, in general the image intensity peak positions may differ from the actual atomic column positions, particularly at defects, and other contrast features may arise due to dynamical scattering that have no one-to-one intuitive relationship to the atomic structure. Hence, it is often necessary to simulate images for postulated atomic structures, accounting for the various parameters associated with the instrument (e.g., focus, convergence angle, lens aberrations) and specimen (e.g., thickness and crystal tilt) in order to meaningfully interpret and quantify the observations. A number of software packages for HRTEM and HRSTEM image simulation are available (e.g., Dr. Probe [68], JEMS [69], QSTEM [70], [71], COMPUTEM [30, 72]).

Once simulated, and appropriately scaled in size and intensity, the images can be compared by evaluating the deviations between simulated and observed peak (or minima) positions or in a more sophisticated manner, by comparing the intensity distributions on a pixel-by-pixel basis. Metrics for comparing the simulated and experimental images include the Normalized Euclidean Distance (NED) [64], the Chi^2 statistic [73], and the R-value [74]. For periodic images, it is often useful to average multiple identical unit cells to increase the signal to noise [64, 65]. Several iterative refinement approaches, which compare the observed and simulated images and then adjust the structure until convergence, have been implemented [64, 73, 74]. The precision of atomic site location depends both on the nature of the image simulation model

and the accuracy of the determination of its parameters as well on the noise and statistical variability in the image itself. Through careful consideration of these factors, rigorous statistical methodologies for establishing the uncertainty bounds for the atom site location have been developed [74-78].

With the increasing possibility of collecting large area sets of atomically resolved data, there comes the challenge of efficiently segmenting this data to identify the location of crystal defects and to assess or classify the defect type or local atomic configuration. Here, microscopy is beginning to draw on visualization and segmentation approaches originally developed in the atomistic modeling community for large atomic simulation data sets. For instance, the centrosymmetry parameter [79], which is widely used for visualization of large-scale atomic simulation, has also been adapted and applied to the analysis of atomic resolution TEM images of crystal defects and interfaces [58, 80-82]. A more quantitative approach for visualizing and characterizing the core structure dissociated dislocations is to compute the local components of the Nye Tensor [83]. This approach has also been extended to atomic resolution TEM observations [84, 85]. Figure 4 provides an example of an experimentally observed dissociated dislocation analyzed using both the center of symmetry and Nye Tensor methods [85].

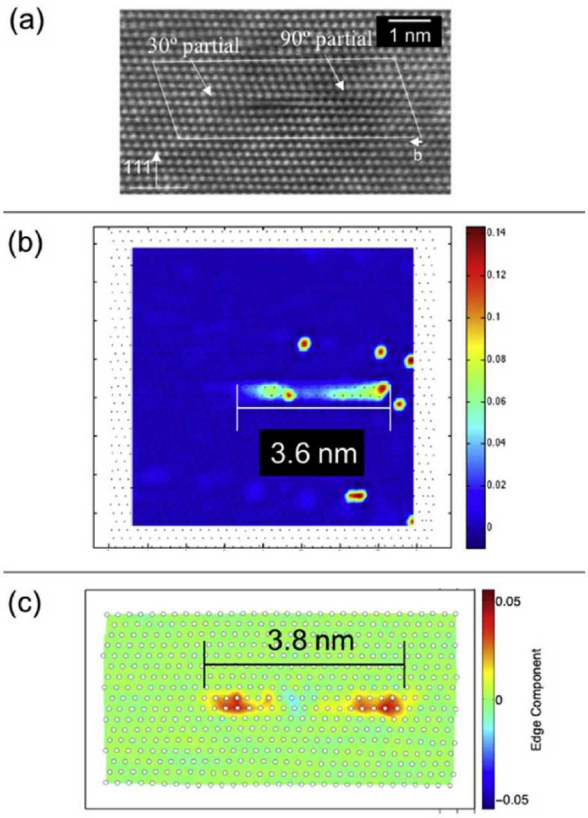

Figure 4. Visualization approaches originally developed for atomistic simulations can also help in visualizing and segmenting atomically resolved experimental images. This example shows an HAADF-STEM image of a dissociated 1/2<110> dislocation in a high-entropy alloy (a). The defect is analyzed using (b) the center of symmetry parameter [79], showing the position of the stacking fault, and (c) the Nye Tensor [83], showing the separation of the partial dislocations. From reference [85].

The limitations of atomic-scale crystal defect analyses in conventional two dimensional projections are being overcome by the emergence of electron tomographic methods with atomic resolution [27]. One approach to extracting atomic resolution 3D information is through electron optical depth-sectioning [86, 87]. In this technique, a highly convergent electron beam, which has a narrow depth of focus, is adjusted to sample different depths of the specimen. This approach has been applied to measuring three-dimensional atomic displacements associated with the screw component of dislocations both aligned with the beam [88] and transverse to the beam [89] and to image buried grain boundary facets [21]. Atomic resolution electron tomography can also be conducted by collecting a series

of images over multiple tilt angles and then reconstructing a three-dimensional atomic representation from the suitable aligned data set. This approach overcomes the limitations resulting from finite depth-of-field optical sectioning approaches but does require specimens stable to the large electron dose obtained under multiple electron image exposures. Examples include analysis of nanoparticle morphology [90, 91], grain boundaries [92], dislocations [93], and measurement of three-dimensional lattice strain [94, 95].

2.3 Strain Mapping from Atomic Resolution Images

The ability to resolve the atomic-scale crystal lattice in advanced microscopy affords the opportunity to directly measure distortions and strain around crystallographic defects. There are two major approaches to such strain measurements. Real space methods for strain mapping most commonly rely on some sort of peak fitting of the atomically resolved lattice and then a comparison of these peak positions with a reference lattice, often fitted to a nominally unstrained region of the image [61, 66, 67]. Alternatively, in Fourier-space methods one computes the Fourier components of the real-space image and then determines the displacements and strain from an analysis of the spatially resolved phase shifts of these components. For either approach, it is critical that the starting image be free of distortions resulting from the imaging process itself as discussed above.

Fourier space methods for strain mapping are useful because they avoid the need for peak fitting while still drawing on the full set of image data. The predominant Fourier-based approach to strain mapping is the GPA method [96]. This approach has been widely applied to the analysis of crystal defects. Examples include work on strains and rotations at twin and domain boundaries [97-99], crystal lattice dislocations in bulk [100] and 2-D [101] materials, grain boundary dislocations [100, 102] and misfit dislocations [103-108]. An example showing displacement fields measured near a dislocation in Silicon is shown in Figure 5.

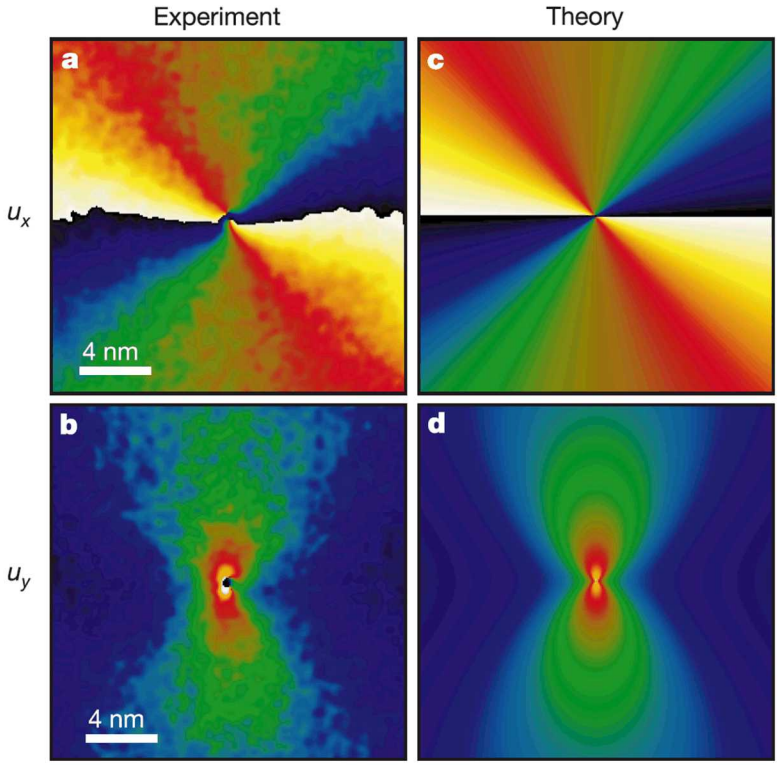

Figure 5. Atomic resolution images can be analyzed to quantitatively measure strain fields in the vicinity of crystal defects. The example here shows displacement fields measured using the GPA method [96] from a HRTEM image of a 1/2<110> dislocation in silicon (a, b). The experimental measurements are compared against the predictions of anisotropic elasticity (c, d). From reference [109].

The basis of the GPA method is to extract spatially resolved Fourier components from an atomically resolved image and to determine displacements and strain from the phase shifts of these components. Specifically, a real-space image, with intensity, I, at position $\boldsymbol{r}$, can be represented by [96]:

$$I(\boldsymbol{r}) = \sum_g H_g(\boldsymbol{r}) \exp\{2\pi i \boldsymbol{g} \cdot \boldsymbol{r}\} \qquad (1)$$

where $H_g(r)$ are the local values of the Fourier components associated with the reciprocal lattice vectors, $\boldsymbol{g}$. To compute the phase image for a specific $\boldsymbol{g}$, the image is Fourier transformed, a mask is constructed around the selected $\boldsymbol{g}$, and then the inverse Fourier transform is computed, giving the complex image that can be expressed as:

$$H'_g(\boldsymbol{r}) = A_g(r) exp\{2\pi i \boldsymbol{g} \bullet \boldsymbol{r} + iP_g(\boldsymbol{r})\} \qquad (2)$$

Here, A_g is the position resolved amplitude and P_g is the position resolved phase. The two-dimensional displacement field, resolved into components along directions *x* and *y*, is determined from the phase images computed from two independent reciprocal lattice vectors, $\boldsymbol{g_1}$ and $\boldsymbol{g_2}$:

$$\begin{pmatrix} u_x \\ u_y \end{pmatrix} = \frac{1}{2\pi} \begin{pmatrix} g_{1x} & g_{1y} \\ g_{2x} & g_{2y} \end{pmatrix}^{-1} \begin{pmatrix} P_{g1} \\ P_{g2} \end{pmatrix} \quad (3)$$

The two-dimensional strain field is then determined by differentiation of the displacement field.

In practice, there are several important considerations for how the data are treated in order to obtain reliable and physically meaningful results from the GPA method. One issue is the potential for artifacts such as spectral leakage since the Fourier transforms are operating on data set of finite extent. This issue is typically mitigated by employing a window function, such as a Hann function, to smoothly attenuate the data at the edges of the image. Another critical issue is the selection of the mask for selecting **g** in the computation of the phase image. With decreasing mask size (in reciprocal space), there is a tradeoff between decreased sensitivity to noise and reduced spatial resolution. An optimal mask diameter (typically chosen with a Gaussian profile) has been recommended at ~0.25g (at FWHM) [110]. The selection of **g** can also be critical. For instance, Peters et al. have shown that large artifacts in the strain measured by GPA analyses of compounds possessing compositionally distinct sublattices due to additional contributions to the phase term [110].

3. Mesoscale Defect Characterization

In addition to better understanding the atomic scale interpretation of HRTEM images and HRSTEM and maps, large data processing also has the potential to greatly enhance the interpretation of defect structures captured by Select Area Electron Diffraction (SAED) patterns and conventional TEM characterization techniques. This section reviews three research areas with great potential for rapid advancements in the coming years. They

include: 1) diffraction pattern simulations from MD simulations, 2)structural defect analysis with a focus on nanometer size defects, and 3) electron holography and tomography to gain a fuller understanding of defect type and location in a TEM foil.

3.1 Electron Diffraction Simulations

Similar to the extensive progress made in coupling atomistic modeling to MD simulations, a similar effort has occurred in coupling MD simulations with electron diffraction characterization. From the modeling perspective, there have been great strides in coupling the SAED and NanoBeam Electron Diffraction (NBED), [111, 112] as well as potentially Precession Electron Diffraction (PED) and BF/DF (Bright Field/Dark Field)STEM maps. This analysis is already incorporated into the Large-scale Atomic/Molecular Massively Parallel Simulator (LAMMPS) [113] and as such provides a direct coupling between any MD simulations and diffraction based characterization. This is similar in nature to the phase contrast simulations that have existed and been refined over the last three decades. [114] An example of the MD and simulated diffraction pattern directly resulting from the LAMMPS diffraction code is seen in Figure 6 for a grain boundary in a simulated Ni sample. [115] The production of such data from the MD code permits rapid and direct comparison to electron diffraction data collected during a TEM study.

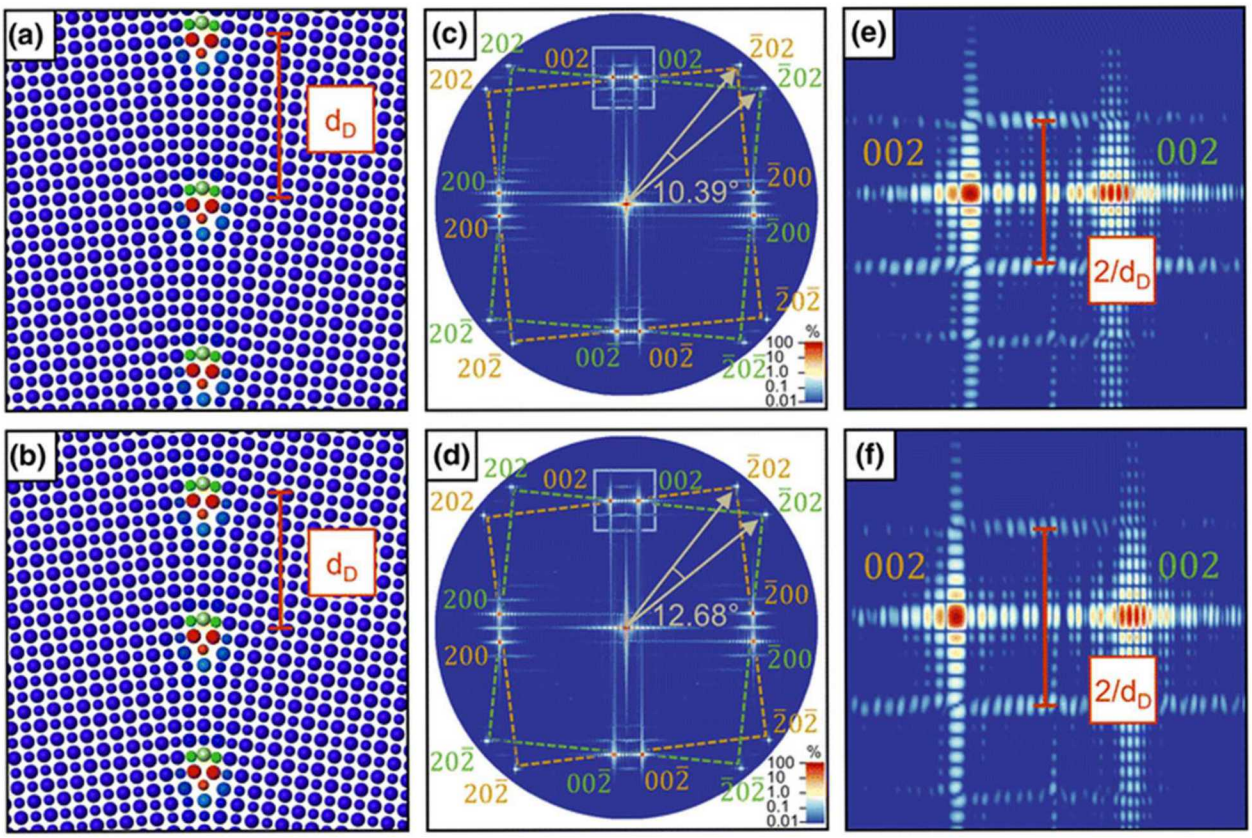

Figure 6. The structure of minimum energy Ni [010] STGBs in MD simulations with tilt angles of (a) 10.39° and (b) 12.68° each created by an array of dislocation cores separated a distance d_D. Simulated SAED patterns aligned on the tilt axis show (c, d) the corresponding misorientation of and (d, e) subsidiary peaks associated with the desolation array near the (002) reflections. From Reference [115].

The ability to created and characterize simulated diffraction data has the potential to simulate experimental conditions during in-situ experiments, as well as directly compare to Precession Electron Diffraction (PED)/ Transmission Kikuchi Diffraction (TKD)/ Electron BackScatter Diffraction (EBSD) (discussed further in section 5) and many other electron diffraction-based techniques. The ideal condition would be if the analysis could be done during the electron microscopy session, so that defect structures in the TEM sample can be characterized on the fly.

3.2 Mesoscale Defect Analytics

Since the original development of TEM, [116] it has been used to characterize the type, density and interactions of structural defects in the TEM foils. These studies have required

not only meticulous Scanning Transmission Electron Microscopy, (S)TEM, alignment, but also often very tedious analysis. In addition, more often than not this detailed analysis cannot be directly inputted into a model and is only loosely compared to the predictive models in the same system. However, the recent emergence of improved control systems during the TEM study and advanced codes for data analytics, this paradigm is rapidly changing. This section in particular will focus on nanometer scale defects located in a microstructure. For atomistic defects see section 2 and for grain and grain boundary characterizations see section 5.

In contrast to optical microscopy and to a lesser extent SEM at their respective length scales, the trusted automation of defect analysis during a TEM study has been extremely elusive. This is in part due to the drastic change in contrast that occurs due to small variations in the deviation parameter that can occur due to small tilting or local bending of the sample [117]. This has been significantly decreased recently due to the development of precession electron diffraction techniques and BF/DF STEM techniques discussed in section 3.1. An extremely difficult experiment is the characterization of dislocation loop type and density in a TEM sample [117]. A recent example of such work that utilized meticulous TEM tilting experiments coupled with image analysis software was completed by Yi et al. in self-ion irradiated tungsten [118-120]. The large amount of dislocation loops characterized in these studies demonstrated the importance of such techniques in understanding the role of processing and environmental conditions on the distribution of defects created. In order to have any level of confidence in the defect density reported, careful attention must not only be paid to the image conditions, but also to the thresholding done during the image analysis. An example of such a threshold in the self-ion irradiated tungsten study can be seen in Figure 7. Such detailed analysis is needed to delineate the contrast due to defects present in the TEM foil from the plethora of other contrast producing artifacts [117]. Currently, this detail is best done by hand and is very much reliant on the expertise and skill of the microscopist performing the thresholding, although work is currently underway on the same data set by Daniel R. Mason and others to automate the analysis utilizing adaptive learning algorithms. Many controversies have arisen in the microscopy community due to unintentional human

errors during the characterization of structural defects from multiple micrographs (e.g. interstitial stacking fault tetrahedra [121, 122]). Many groups across disciplines are implementing various forms of machine learning and other algorithms to improve the thresholding and interpretation of electron micrograph analytics for a wide range of TEM samples and imaging conditions [123-125].

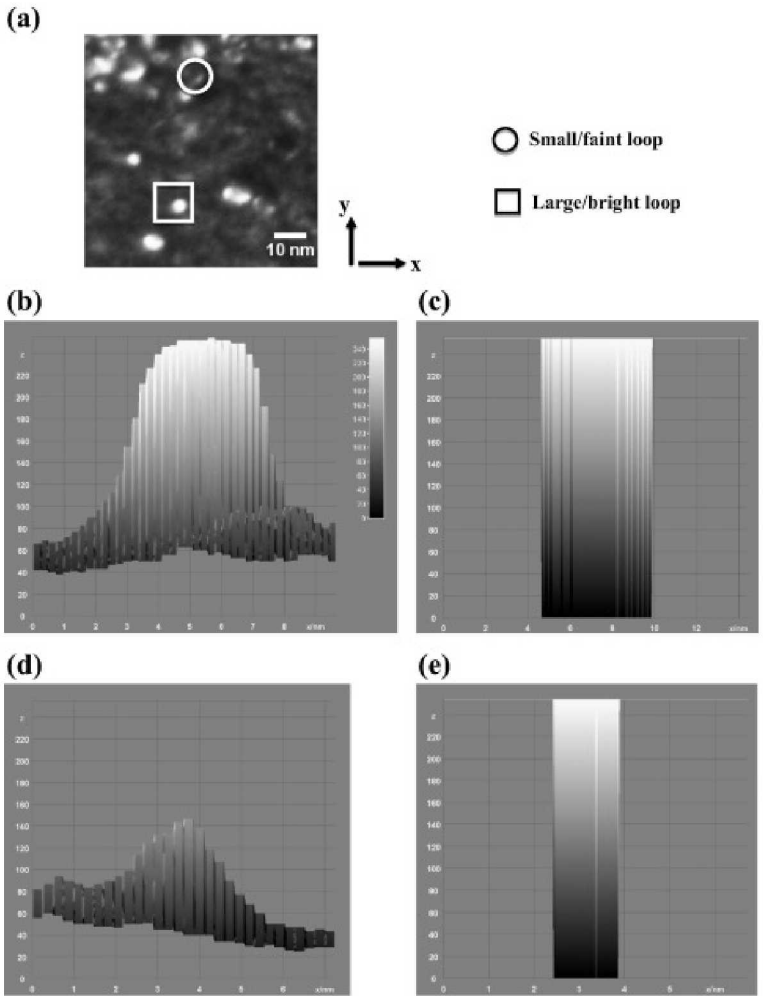

Figure 7. Demonstration of loop sizing in an irradiated pure W specimen with 3D surface plots constructed on the same intensity scale (viewed in the x–z "intensity" plane) [65]: (a) the original grey scale image; 3D surface plots profiles of a large/bright loop in (b) grey scale and (c) binary format respectively; 3D surface plots profiles of a small/faint loop in (d) grey scale and (e) binary format respectively. From Reference [120].

In addition to the direct defect counting, the rapidly improving data analytics that can be obtained provide the ability to better couple TEM experimental observations with atomic and mesoscale models. This chapter will only highlight some of the recent advancements in this coupling. Readers are encouraged to explore the recent review by J. Marian et al. for a deeper exploration of modeling and experimental coupling at the nanoscale. [126] This coupling has been driven by both the modeling and experimental efforts. There has been an exciting effort led by De Graef et al., at Carnegie Mellon University to directly simulate BF/DF TEM micrographs from strain maps that can be produced from most mesoscale simulations. [127-129] The combinations of these modeling approaches should permit direct coupling between atomistic and mesoscale modeling to a large range of (S)TEM based techniques. The current barrier limiting the further coupling of (S)TEM experiments and atomistic and mesoscale modeling is the extensive resources needed to complete any of the coupling described above. We predict with increasing microscope control, improved algorithms, and better transfer of variables that such coupling will become increasingly more commonplace.

3.3 Electron Holography and Tomography

The improved automation of TEM controls and the efficiency of handling large data sets in a smart fashion over the next few decades should provide the ability for uncommon TEM techniques to be automatically incorporated into the alignment of the TEM or implemented upon request. Two such techniques that can be integrated into normal TEM characterization are in-line electron holography and electron tomography. In-line electron holography entails the collection of a through-focal series that is then processed to map out the phase shift present in the region observed. An example of electron holography of cavities in an aluminum TEM foil can be seen in Figure 8. [130] The phase shift map can then be associated with a range in local structure and property variations present in the sample. Such through focus series required to produce in-line electron holography maps are collected manually or automatically every time the TEM focus is aligned. Presently, these through focus sets are rarely converted to in-line electron holography maps due to the complexity and computational resources for such an undertaking.

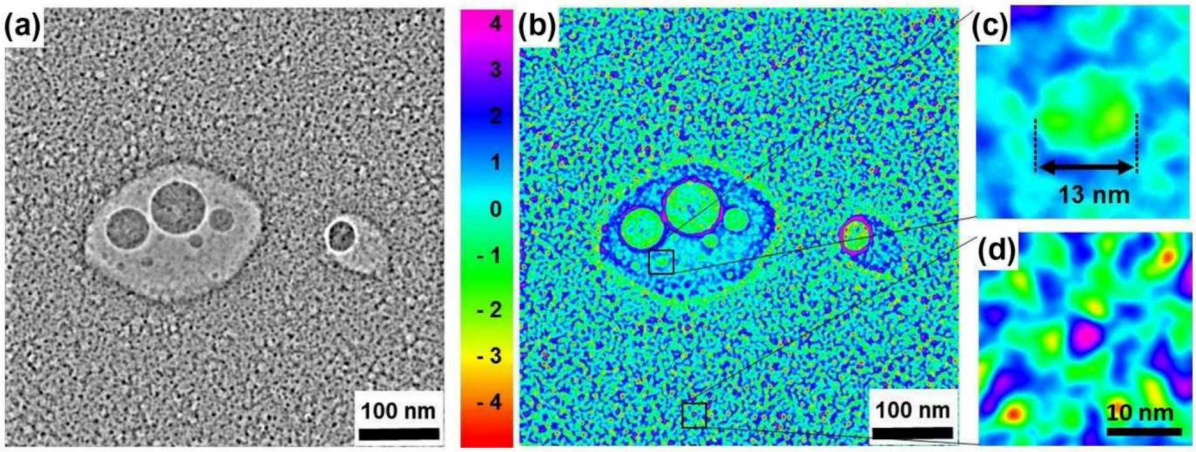

Figure 8. Phase map of cavities in al TEM foil retrieved from the focal series using the in-line holography method, in (a) grey level, and (b) color displays. The scale in Figure 8 (b) refers to the phase shift measured in radians. On the right side, high magnification on phase image details: (top) a cavity of about 13 nm formed at the precipitate/matrix interface, the associated phase shift is ~1rd (green on the color scale), (bottom) nanoscale cavities in the matrix (negative phase shift) and domain with positive phase shift (violet on the color scale) further interpreted as interstitial cluster. From Reference [130].

Similarly, one of the methods already utilized to set the eucentric height of the TEM sample in modern TEMs is small angle calibrated tilting of the goniometer. If during this procedure calibrations images were taken at multiple tilts, an image set required for electron tomography reconstruction would be possible. The ability to do automated electron tomography is significantly more advanced than many other electron microscopy techniques due to the high demand to understand the three-dimensional aspect of the inherently projection image. This development in amorphous materials is significantly further along than for crystalline samples due to the large and concentrated effort from the cryoTEM and biological community [131, 132]. However, some very nice examples of thorough and painstaking electron tomography results in crystalline samples have been achieved. Figure 9 is an example of radiation damage present in a wedge shaped Mo sample taken in WBDF by Li et al. [133]. A full tilting experiment of this sample was completed. This clearly demonstrates the defect denuded zone near the top and bottom surface of the sample, as can be seen in Figure 10, which can also be directly correlated

to the defect distribution predicted by MD simulations of a virtual TEM sample exposed to equivalent Primary Knock-on Atom (PKA) damage [133-135]. Efforts like these demonstrate the potential impact to understand the factors governing microstructural evolution, as well as overcome some of the traditional limitations of TEM characterization but are rarely completed due to the time and effort required to properly analyze the data. Expected advancement and applications of machine learning and similar algorithms should greatly assist in the handling and smart processing of such micrographs.

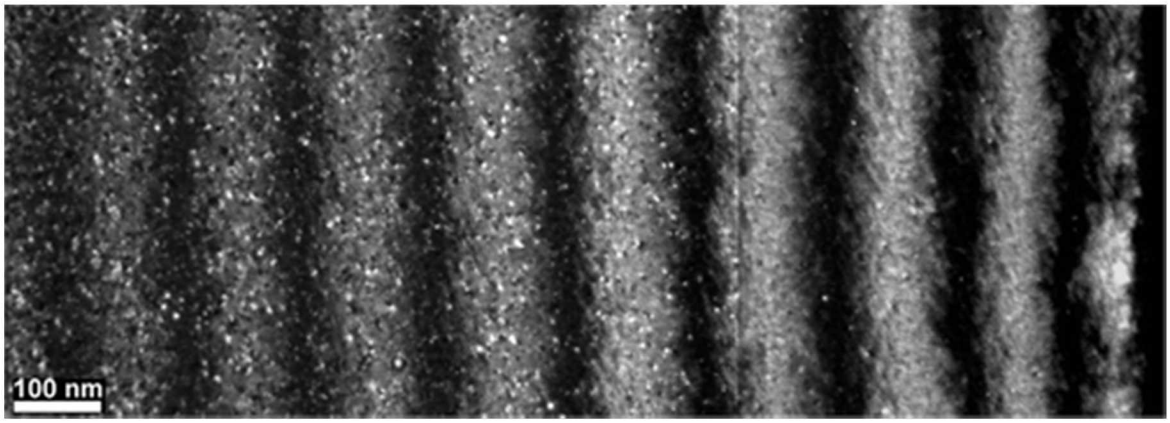

Figure 9. Weak beam dark field (WBDF; g, 5 g) images of the same specimen area showing defect cluster accumulation as a function of dose for Mo in situ irradiated up to 5×10^{12} ions/cm^2 (~0.015 dpa) with 1 MeV Kr ions with a flux of 1.6×10^{11} ions/cm^2/s (~$5 \times 10-4$ dpa/s) and at 80°C. From Reference [133].

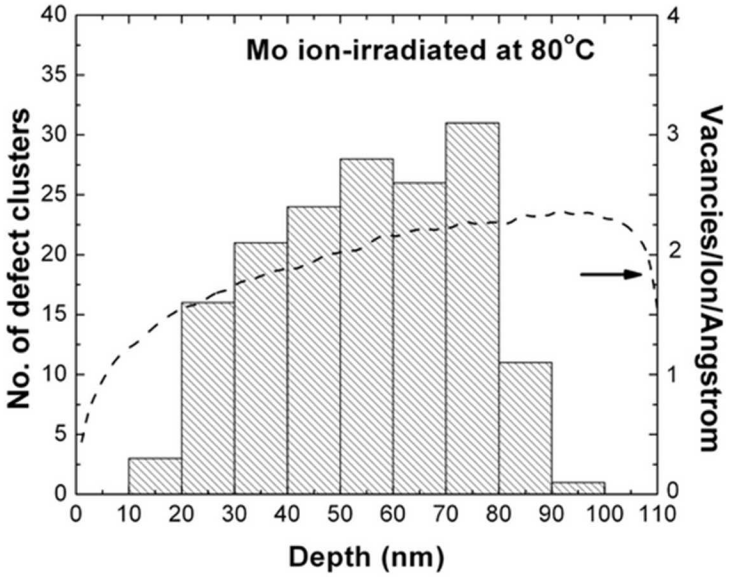

Figure 10. Size distribution of defect clusters as a function of foil depth in Mo irradiated to 5×10^{12} ions/cm^2 (~0.015 dpa) at an ion flux of 1.6×10^{11} ions/cm^2/s (~5×10^{-4} dpa/s) and 80°C with 1 MeV Kr ions (a) foil depth of 0–40 nm, (b) foil depth of 40–70 nm, and (c) foil depth of 70–110 nm. From Reference [133].

As we hope is evident in this section, the recent advancements in mesoscale defect characterization is just the beginning of a much deeper understanding of the defect type, density, and 3D distribution in a sample due to the rapidly advancing capability to characterize and process large data sets. The sub-fields of 1) diffraction pattern simulations from MD simulations, 2) structural defect analysis with a focus on nanometer size defects, and 3) electron holography and tomography are all posed to have rapid growth in the coming years to increased data processing and automation.

4. Time Resolution

To date, there have been three major advancements to enhance the temporal resolution of electron micrograph acquisition. These include, in order of significance: 1) development of direct detection CMOS based cameras, 2) the development of the Dynamic Transmission Electron Microscope (DTEM), and 3) the development of the Ultra-Fast SEM and TEM (UF-SEM or UF-TEM). These three options were envisioned, designed, and developed over the last few decades to decrease the electron dose that beam

sensitive samples are exposed to during imaging, increase the maximum temporal resolution possible during an in-situ electron microscope experiment, or both simultaneously. The remainder of this section will describe the historical evolution and details of each design concluding each subsection with a discussion on the potential for increased capabilities through enhanced data processing routes.

4.1 Solid State Cameras

It was only a little over a decade ago that the debate in electron detectors resolution and general capabilities was between film and CCD imaging. [136] During this time period, the CCD camera expanded to become the system of choice due to the ease of use, ability to check image quality quickly, improved safety, and decreased environmental costs compared to film for most applications. However, at the same time that CCD cameras were dominating, CMOS-based monolithic active pixel sensor (MAPS) detectors were being developed for space applications [137] and then for ionizing radiation applications [138]. This trend continued with a paper that's title included 'new eyes for science'. [139] This was the turning point as shortly thereafter the options and capabilities of direct detect cameras rapidly grew for transmission electron microscopy. [140]

This disruptive evolution in detector hardware technology has created both a crisis and opportunity in the field. The crisis arises from being able to quantify the quality of the data produced by the new cameras, as well as properly handling and processing all of the data produced per experiment. The concerns about detector quality as a function of time was best described by G. McMullan et al. who said "performance of these new detectors needs to be carefully monitored in order to optimize imaging conditions and check for degradation over time. We have developed an easy-to-use software tool, FindDQE, to measure MTF [Modulation Transfer Function] and DQE [Detective Quantum Efficiency] of electron detectors using images". [141] However, if the new artifacts are properly understood and accounted for, similar to the dark field correction to remove the honeycomb overlay present in all CCD images, the direct detect technology has many significant opportunities. These include drastically increasing the spatial resolution

possible under low electron flux imaging conditions (DQE up to 80%), while also decreasing the temporal resolution in the range of 400 frames per second (fps).

Many state-of-the-art research advancements have been possible due to the expanded opportunities provide by the direct detection systems. An example of direct observation of nanoparticle evolution during high resolution observation at a 2.5 ms frame rate can be seen in recent work done by E.A. Stach et al. (Figure 11) [142]. In a similar manner, the state-of-the art has been advanced in many applications with the low electron dose environment and rapid imaging sequence provided by the direct detect systems. These range from near-atomic-resolution single-particle cryo-EM studies [143] to rapid image sequencing of the deterioration of the metal/oxide interface that is the core of corrosion and many other fields [144].

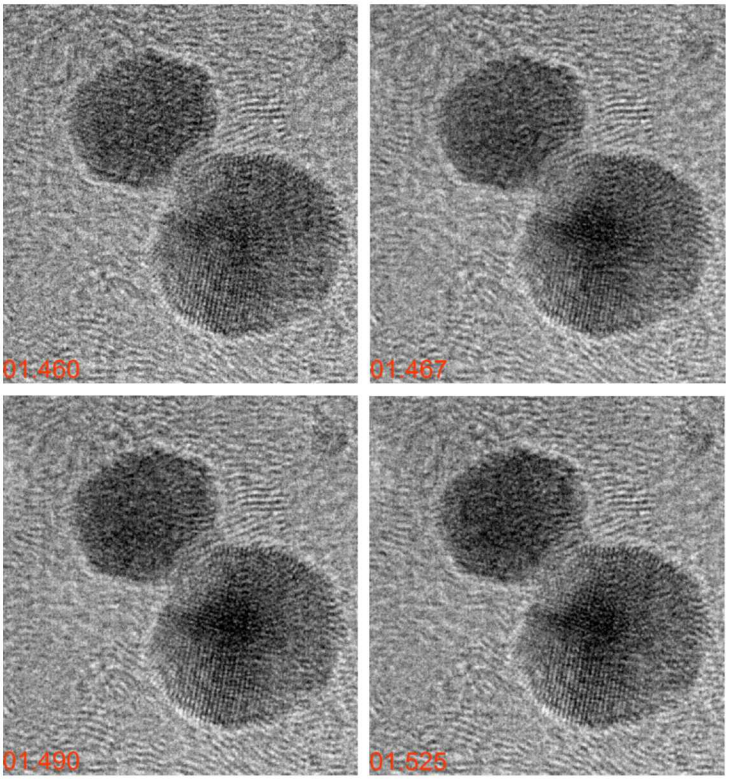

Figure 11. Phase contrast images of the sintering of Au/Cu nanoparticles. The images were obtained at a 2.5 millisecond frame rate in a continuous video stream. Individual images that capture the dynamic changes occurring at the interface during sintering are shown. From Reference [142].

The large amount of data produced by the advancements in TEM camera systems requires the implementation of smart data processing. This development of proper protocols and programs to handle the data is still very much in its infancy but has great potential. As opposed to the continuous collection of data, the current software permits the temporary storage of data with key recent past segments (~seconds) pushed to long term storage on the user's command. This is just one of many data issues and possible tricks to automate around the large quantity of data produced by this transformative TEM camera technology. [145] However, the development of strategies focused on how to best handle the data is not taking full advantage of the possible new areas of research permitted by this hardware advancement. An example of such development of new techniques utilizing direct detection systems is the rapid development of in-situ STEM based techniques spearheaded by scientists at the National Center for Electron Microscopy (NCEM). [146] The core concept with this approach is to minimize the use of post samples apertures and fast detectors; thus, collecting as many electrons leaving the TEM foil as possible during a STEM scan. This provides virtual BF, virtual DF, and HAADF images among other potential data simultaneously. An example of such work exploring the local strain mapping of a GaAs/GaAsP system can be seen in Figure 12 [147]. Increased capabilities through enhanced data processing routes provide the ability to characterize nanoscale changes in strain maps like those in Figure 12 during complex in-situ experiments. [148] The ability to apply this to a range of in-situ (S)TEM goes significantly beyond these initial studies, and as a result, opens a range of new connections between experiments and modeling efforts.

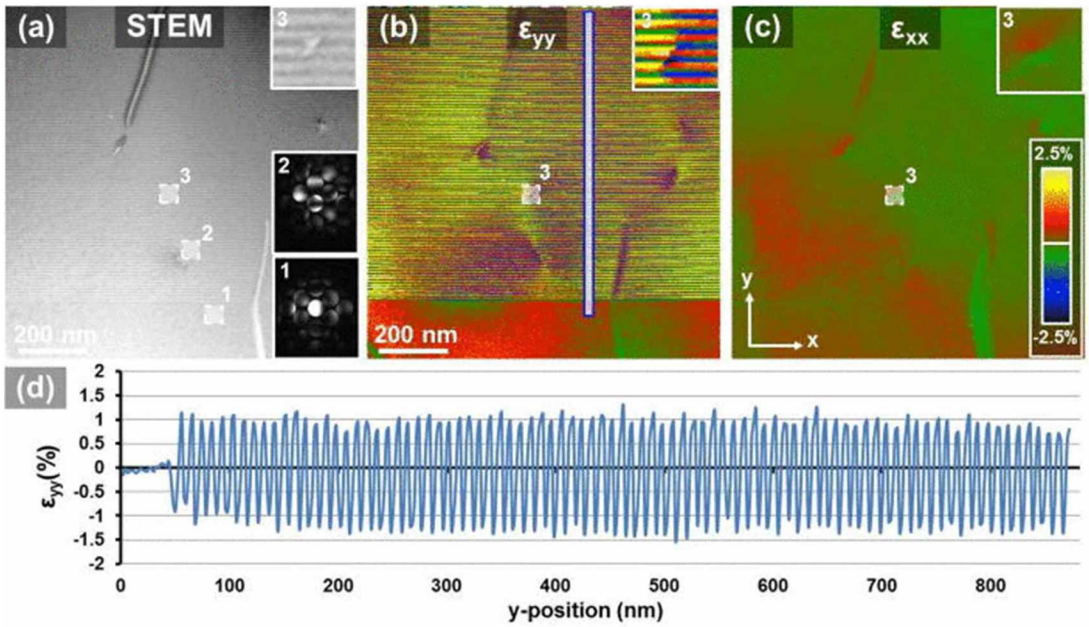

Figure 12. NBED analysis of a GaAs/GaAsP multilayer device cross-section across a large 1 μm FOV. (a) HAADF image of the analyzed section. Insets are CBED patterns taken from areas 1 and 2 showing the misorientation possible to analyze with the technique. Inset labeled 3 is a short-range stacking fault. (b) NBED strain map of ε_{yy} strain where y is the [002] direction. (c) NBED strain map of ε_{xx} strain where x is the [220] direction. (d) a ε_{yy} profile scan across the entire device as indicated by the vertical box in (b). From Reference [147].

4.2 DTEM and UFTEM

The effort to advance the temporal resolution of TEM experiments does not stop at the 400 fps range, but advances down into the nanosecond and picosecond regime through the development of dynamic TEM (DTEM) and ultra-fast TEM (UFTEM), respectively. Both of these techniques have greatly evolved over the last two decades through rapid advancement in the coupling of laser innovations and TEM optics. Both types of system utilize a laser to excite the cathode and control the release of electrons and a pump-probe design to explore the properties of the sample. The two technologies provide different but complementary capabilities. The DTEM is designed for non-reversible processes and as a result an adequate number of electrons must be produced from every burst of electrons. In contrast, the UFTEM is designed for reversible processes and the images can be

added to provide suitable image resolution with improved signal-to-noise. Over the last decade the DTEM system has evolved from the collection of simple single diffraction patterns or bright field images [149, 150] to a complex “movie mode” design where a small set of images (9, 16, etc.) is collected on a single large CCD detector by deflecting the electron at the bottom of the projector system [151]. In a similar manner, the ultra-fast electron microscopy field developed from the Noble prize winning work by the Zewail group in ultra-fast electron diffraction [152] through a range of UFTEM design and strategies [152-154] to current versions of an UF-Field emitter TEM design[155] and UF SEM capabilities [156, 157]. Both DTEM and UF-TEM system hardware development has been impressive. However, both demonstrate the need for smart data processing to improve data integration, deconvolution, as well as timing determination and control. If improvements can be made to improve the integration and automation of the control system, along the lines of that underway for AC-TEM systems, significant opportunity for main stream introduction of DTEM and UFTEM will be possible. Similarly, a direct and efficient way to handle and process the large and convoluted data sets produced by these techniques would greatly advance the applications with picosecond reversible and nanosecond irreversible dynamics.

5. SEM and X-Ray Mapping Techniques

In recent years, several advances have been made in SEM, optical microscopy, and X-Ray techniques. These include: (1) faster imaging and larger images through montages, (2) Strain measurements through digital image correlation (DIC), (3) orientation imaging such as Electron Backscatter Diffraction (EBSD) and Transmission Kikuchi Diffraction (TKD), and (4) Improvements in speed and resolution of X-Ray Computed Tomography (XCT) and the use of XCT for Digital Volume Correlation (DVC).

5.1 Electron Microscopy

5.1.1 SEM

At the microscale, a single electron microscope image is often the size of a single grain. To take advantage of the high-resolution imaging capabilities, yet still obtain statistically-significant regions of interest, image montaging (combining multiple images into a single large image) is often employed. In some cases, a large pixel-count camera would largely address the problem; however, such large sensors are often unavailable. Furthermore, researchers with a large sensor would likely still stitch together images and data sets because the demand for large data sets vastly outscales the current sensor pixel counts by several orders of magnitude. Most scanning electron microscopes have software to perform such image stitching but they typically do not have stitching accuracy sufficient for DIC. Stitching images can also take considerable time if large regions are to be imaged successively (e.g. at each load level for in situ testing). One area in which data processing of SEM image montages is making an impact is in fracture surface analysis. Large montages can be used to characterize void fractions on fracture surfaces in high-porosity additively manufactured samples. Each fracture surface can be completely covered with high enough resolution to discern important details such as fracture origin, pores, or inclusions. The ability to examine of dozens of specimens like this in an automated way will likely impact statistics of tensile tests.

5.1.2 Multiple Beam SEMs

One solution to obtaining very high resolution images over large regions is a multibeam SEM system [158]. These systems currently integrate up to 61 or even 91 electron beams into a single microscope. Each beam is used to image a tile, and tiles are montaged into larger images (Figure 13). In a typical scan, a pixel size of 4 nm can be used to image an area of a square centimeter in a matter of a few hours. A single square centimeter at this resolution corresponds to a 625,000 *Megapixel image*! Consequently, data transfer, storage, and analysis become significant undertakings. Fiber optic connections with

dedicated servers are necessary. Due to the slow speed of long distance data transfer, it is often faster to physically ship hard drives with data than to transfer data electronically.

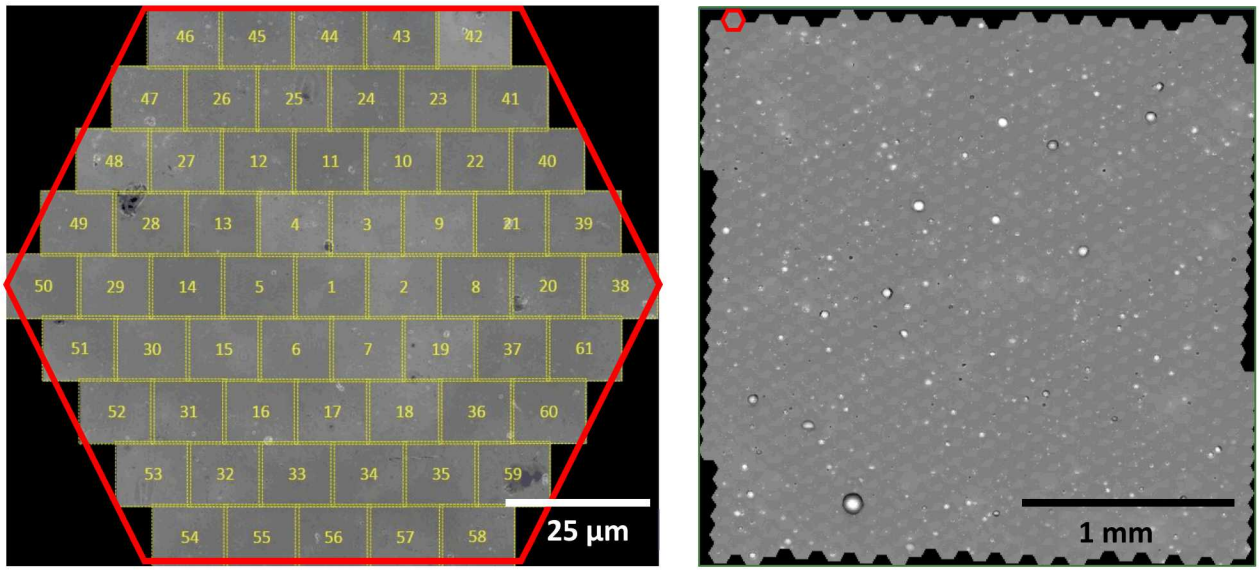

Figure 13. (Left) An image pattern from a multi-beam SEM. In this case, 61 rectangular images are tiled to form an approximate hexagon shape. (Right) Many of those hexagons (same region outlined) are then tiled to image large regions. (Courtesy of Joseph Michael, Sandia National Laboratories)

The potential of multibeam SEM systems is promising. However, harnessing this potential requires significant effort. Processing such large datasets necessitates the need for algorithms and parallel computing rather than individual analysis by researchers as has been done throughout the history of materials science. Thus far, this data has only been analyzed with simple algorithms such as searching integrated circuits for flaws. [158] Early work has been done in using multibeam SEMs to search for pores in cross sections of additive manufactured materials (Figure 14). The advantage of this system is apparent; all flaws larger than ~400 nm can be identified within regions encompassing several square millimeters.

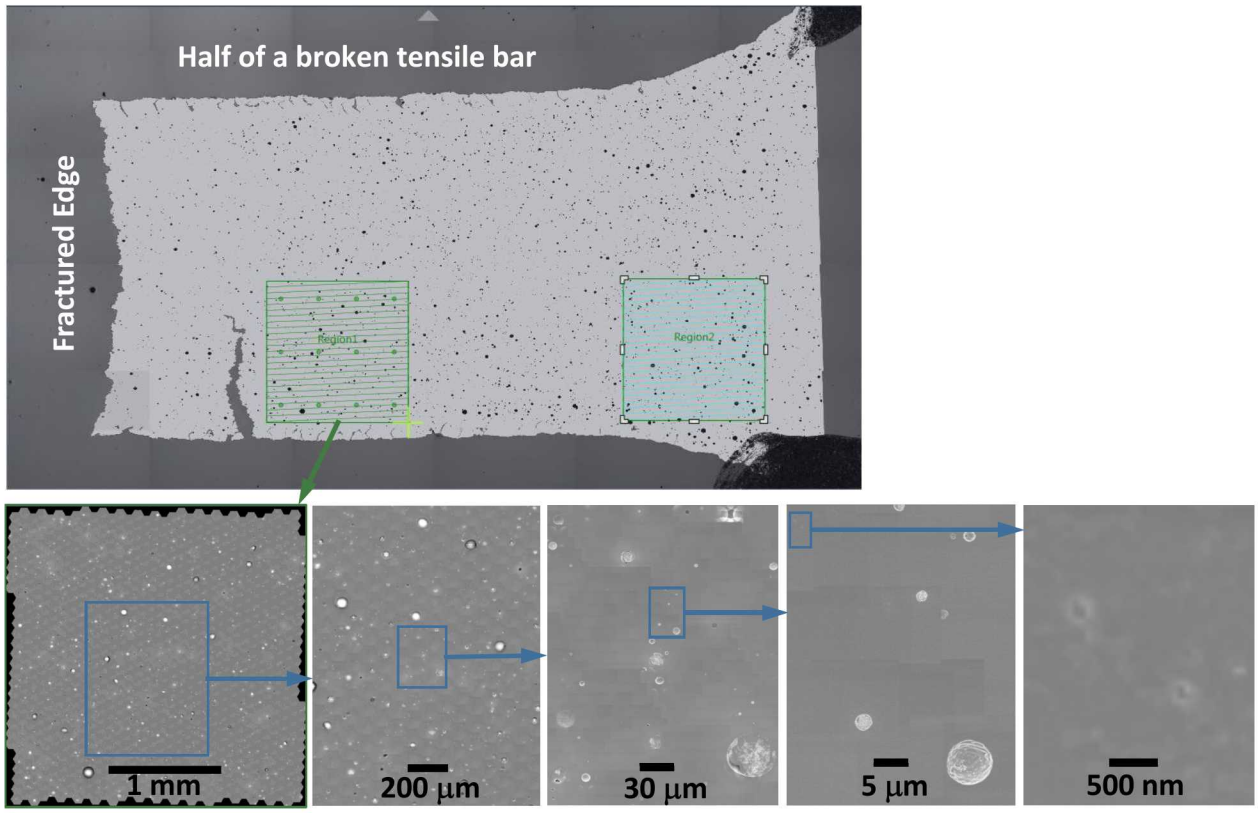

Figure 14. Multi-beam SEM imaging of a broken additive manufactured specimen with widespread porosity. These images can be used to characterize porosity distributions from sub-micrometer voids and larger. (Courtesy of Joseph Michael, Sandia National Laboratories)

In addition to flaw detection, these microscopes have great potential for characterizing microstructural phenomena over large scales for statistical analysis. One such technique is microscale high resolution digital image correlation (discussed in a subsequent section). At this time, sufficiently fine speckle patterns cannot be generated to take advantage of this imaging system, but they certainly will be in the coming years.

Multibeam SEM systems do have some drawbacks that should be noted. Artifacts such as ghosting from nearby tiles and contrast variability are common. Furthermore, these currently only work with secondary imaging on flat specimens. This limits the types of experiments that can be performed since secondary imaging often brings out surface topography.

5.2 DIC

5.2.1 Full-field implications for modeling

The development of digital image correlation (DIC) in the 1980's [159] was a major driver towards digital full-field data in the materials science community (along with EBSD and grid techniques). Digital image correlation began to replace its full-field predecessors such as moiré interferometry and photoelasticity due to its wider applicability and relative ease of use [160]. DIC has a particular advantage for microstructural scale experiments over preceding techniques due to its lack of an inherent length scale; it can be used on images from nanometer to kilometer scales.

Several different approaches can be taken to work with these large, full-field data sets. The simplest and most common approach is to plot the fields for display purposes; this approach is useful, but is rarely the most effective use of large data sets. The goal of data science is to leverage rich data sets (combinations of multiple sets of data, for example) to better understand the phenomena being observed. A micromechanics example of this is the alignment of EBSD measurements of crystallographic orientation with full-field strain measurements from digital image correlation [161, 162] in Figure 15. Aligning fields of data from separate techniques is a powerful approach that will be necessary for making progress in materials science going forward. This method is quickly becoming one of the dominant methods for informing and validating crystal plasticity models.

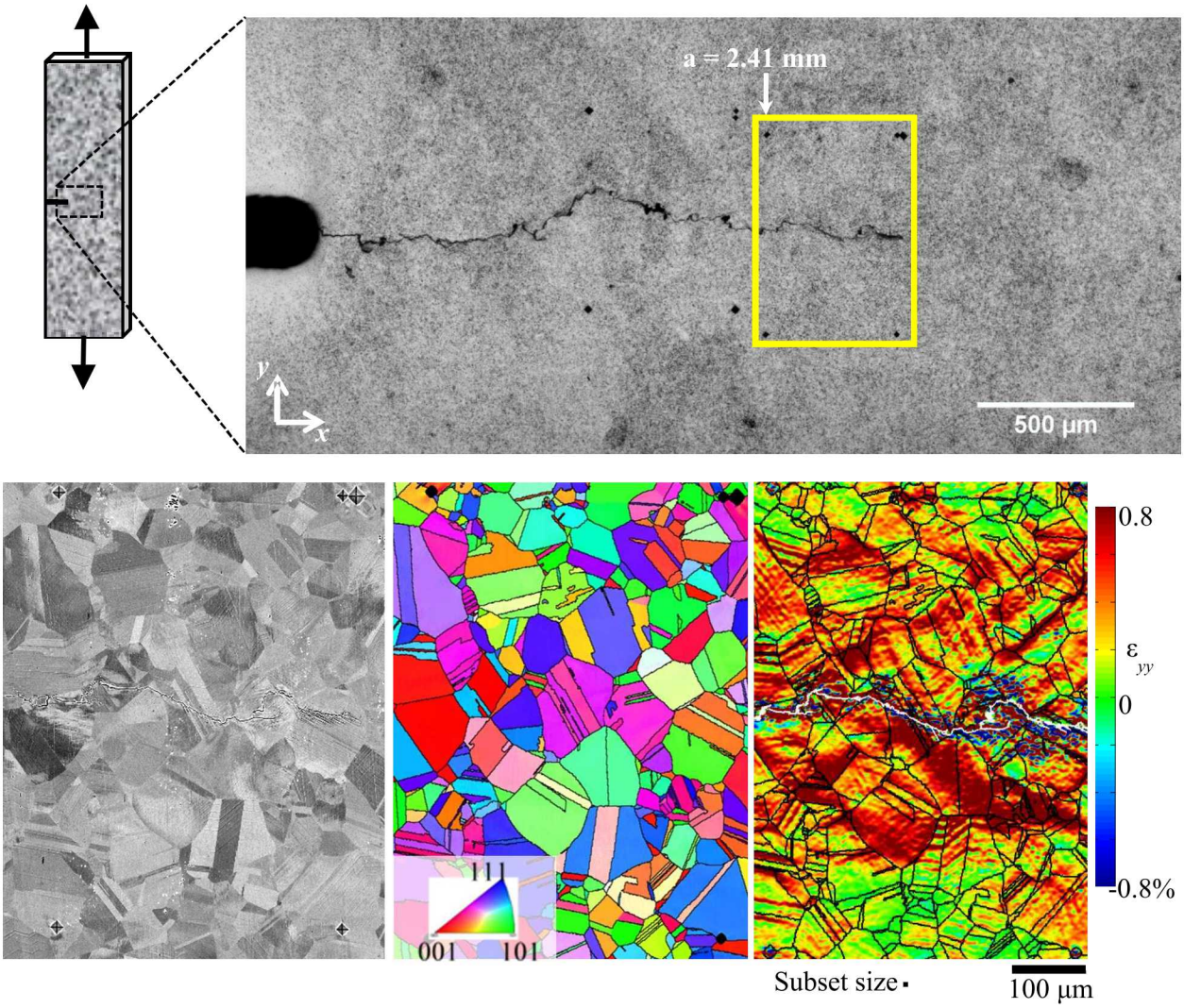

Figure 15. An example of aligning multiple data sets (taken from [173]). (top) A speckle pattern on a fracture specimen was imaged to observe a fatigue crack's growth relative to the microstructure. A small region around the crack tip was imaged using (left to right) backscatter electron imaging, EBSD, and DIC strain fields (in the vertical direction). In the DIC map, grain boundaries from the other two maps are overlaid.

A more involved data-science approach to these full-field data sets is to perform collocation (least squares regression) analysis to extract parameters that describe the displacement field such as a stress intensity factor near a crack [174, 175]. This has been done using DIC data [174, 175] and using data obtained from other approaches such as moiré interferometry, photoelasticity, and holography [176, 177]. An example of

collocation of DIC data around a crack tip with the analytical solution is shown in Figure 16.

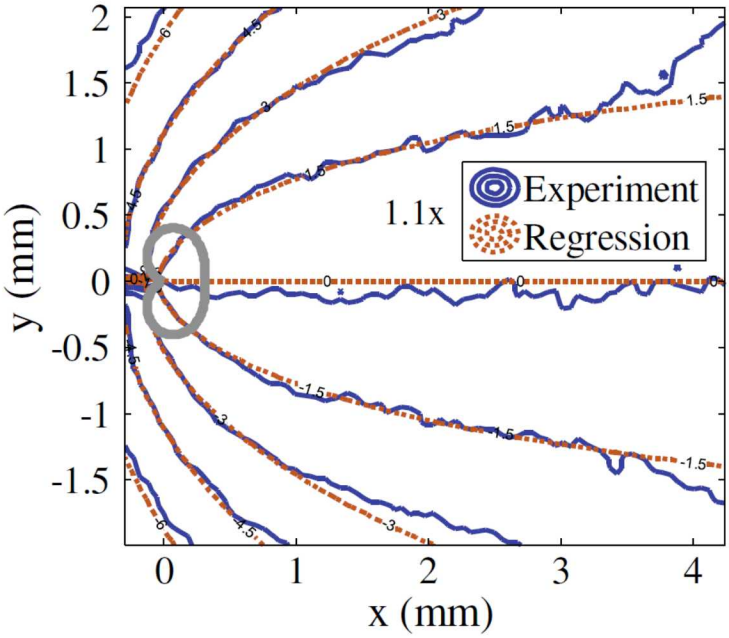

Figure 16. Example of the collocation technique on a vertical displacement field around a crack tip. Parameters such as the stress intensity factor, T-stress, rigid translation, and rigid rotation are chosen to minimize the error between experimental measurements and the model displacement field. Taken from [174].

Yet another approach to handling full-field data sets has been to exploit the varying nature of stress and strain fields in complicated geometries to provide rich data sets for model development. One approach to this has been the virtual fields method championed by Pierron and Grediac [178]. The virtual fields method employs specimen geometries that have a wide variety of stress and strain states throughout the specimen. By using the principle of virtual work, the model fits these multiple stress/strain states to extract material parameters. This technique is currently in the early stages and is being used for macroscopic material models [179] currently; however, it shows promise for application at the microscale. Undoubtedly, more complex approaches will be developed towards understanding microscale behavior by applying machine learning techniques such as data science or neural networks to large experimental and simulation data sets.

In addition to various plasticity models that predict material's physical properties, computational models to accurately reproduce microstructural features and their defects in polycrystalline materials are being developed and coupled to multi-scale experiments. For example, kinetic Monte Carlo [163] or phase field [164, 165] based techniques are used in grain growth simulations to reproduce realistic RVEs of polycrystalline microstructures. It has been shown that accurate representations of polycrystals are required for high fidelity polycrystalline simulations in both atomistic and continuum scale simulations [166, 167]. More recently, concepts and toolsets from data science are being adopted in computational materials science. For example, reduced-order models [168, 169] or database-driven approaches [170-172] are developed to avoid computationally expensive simulations or to establish efficient process-structure-property relationships.

5.2.2 HR-DIC

The incessant drive for images with larger pixel counts is acutely felt in the DIC community, in which each pixel directly represents more data. Due to the nature of DIC, increasing pixel count, even without any direct improvement in measured resolution (i.e. limited by the speckle size) will provide improved accuracy due to the fact that the technique averages over large numbers of pixels for each subset. However, a more typical use of increasing pixel count is to shrink the speckle size to obtain finer resolutions and improved accuracy over larger areas. DIC derives its subpixel accuracy (typically less than $1/100^{th}$ of a pixel) [180] from averaging the motion within square subset regions of many pixels. A typical subset size for small scale DIC might be 51 x 51 pixels, meaning that 2601 pixels are analyzed to obtain the strain value at a single data point. If the pixel count is doubled without modifying the speckle pattern, an equivalent subset size would be approximately 101 x 101 pixels. Therefore, the same subset region would be analyzed with four times as many pixels, 10,201, resulting in better averaging of pixel positions and more accurate DIC displacement and strain values. Of course, this improvement comes at a cost—four times as many pixels need to be captured at the increased magnification to cover the same area. Additionally, extra processing time and storage are required to analyze the considerably larger pixel counts.

In many cases, the extra resources required to analyze large pixel count images (~40MPix) with DIC are worth it. Performing DIC on high pixel count images has been termed “High Resolution Digital Image Correlation” (HR-DIC). [181] The tradeoffs and techniques for performing HR-DIC were outlined in. [161] Performing DIC on stitched images has been shown to leave noticeable strain localizations (or discontinuous displacement) at the stitching boundaries. There appears to be no solution other than modifying the greyscale values in the tiles themselves or performing DIC on each tile before stitching. The latter would be easily accomplished with parallel processing, which is starting to be introduced into standard DIC software packages.

5.2.3 Micro-Scale DIC

Performing DIC on SEM images (SEM-DIC) is particularly appealing for understanding microscale behavior such as crystal plasticity. Although some research has been done optically, [182, 183] many of the microstructural phenomena of interest (e.g. sub-grain-scale deformation, twinning, slip bands, etc.) are near the limit of optical microscopy or below it. SEM-DIC can be particularly challenging due to the multiple sources of image distortion. At low magnification, many SEMs are designed in such a way that fisheye distortions, pincushion, or other non-symmetrical distortions are present. This is typically due to a non-uniform rastering speed of the electron beam as it traverses the image. At higher magnifications (fields of view less than 30 μm assuming an image width of ~1000 pixels), lens distortion effects decrease, but drift distortion increases in significance. [184] With current hardware and software limitations, there tends to be a range of moderate magnifications (fields of view around 30 μm to 500 μm) at which neither of these distortion types appears to add much error to DIC measurements at moderate strain levels. While avoiding SEM-DIC distortions may be the expedient approach, a formal approach to correcting for the distortions was described by Kammers and Daly [184]. Lens distortions can be corrected through a rigid motion test on the specimen. Drift distortions can be corrected using a surrogate sample and taking images at successive times.

HR-DIC techniques have proven particularly useful to understand grain-scale phenomena, often through the development of crystal plasticity models. One example of microstructure-aware plasticity models that is gaining momentum is the Crystal Plasticity Finite Element Model (CP-FEM). CP-FEM models utilize crystal plasticity constitutive equations that describe mechanical behaviors of single crystals, and their aggregate behaviors are simulated within a finite element method (FEM) framework. In these models, initial states of microstructural features such as grain morphology and crystal orientations are often informed from EBSD data [166-169] to predict evolutions of textures [167, 170-175], dislocation densities and cell structures [176-180], grain boundary effects [176, 181, 182], and heterogeneous intra-grain surface strain fields [167, 174, 175, 183, 184]. An extensive overview of CP-FEM model can be found in [185]. Figure 17 shows one example of direct comparisons of surface strain fields using CP-FEM predictions and DIC measurements [167]. A conventional CP-FEM model accurately predicted heterogeneous sub-grain scale strain fields, while more detailed microstructural features such as slip lines and grain boundary were not captured.

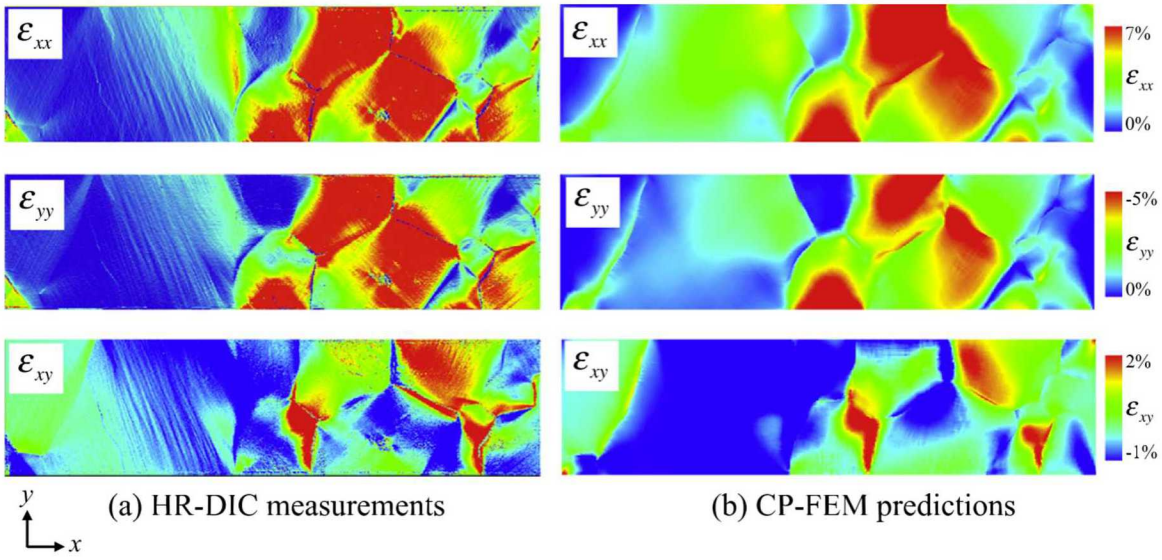

Figure 17: A comparison of measured and predicted surface strain fields of tantalum oligocrystals after 3.4% deformation in tension. From Reference [185].

5.3 Orientational Imaging

5.3.1 EBSD

Electron Backscatter Diffraction (EBSD) has dramatically changed the fields of crystallography and crystal deformation. Traditionally, X-ray diffraction only provided measurements of macrotexture. The full-field nature of EBSD allows for microtexture analysis which is powerful for understanding grain-scale phenomena. As discussed earlier, EBSD is being leveraged with DIC to develop improved crystal plasticity models. The technique is finding increased utility with the need to characterize microtexture in additive manufactured materials. At the moment, the exact influence of build parameters on microstructure is not well understood. Consequently, the microtexture in additively manufactured components can vary dramatically compared to conventionally processed components. EBSD will be instrumental in relating the processing parameters to the resulting microstructure. The large number of build conditions will make EBSD on additive manufactured specimens a big-data problem. Each printed material has a different pedigree, even if it is as slight as being at a different build plate location. Consequently, tracked metadata will need to be linked to additive manufactured materials including their crystallographic data. Efforts to this effect are currently underway by a large number of organizations including the National Institute for Standards and Technology (NIST), Granta Design Limited, ASM International, and a number of United States National Laboratories among others. Saving raw EBSD data, metallography images, etc. on each sample is currently difficult to choreograph, even if storage is available. Developing metrics to succinctly represent such data will be necessary for storage, handling, analysis, and archiving [186].

On top of these data challenges is an increase in the inherent size of the EBSD data. Ultra-fast EBSD systems have recently been developed [187, 188] that can index up to 3000 points per second, several orders of magnitude faster than speeds available just a few years ago. With this capability, it is now possible to measure the full microtexture

throughout the cross section of a component on the scale of inches. This data could help decision making, particularly in the processing realm, again with the challenges of data management. This approach will likely become more intensive as serial sectioning EBSD approaches become more automated. Already, there are automated systems to serial section and image through a specimen, but it is often limited to optical microscopy images. Techniques that can provide high throughput serial sections of EBSD data via conventional grinding, plasma-based Focused Ion beam (FIB), and femtosecond laser are in development. If made fast enough, these techniques would provide scientists and engineers with a full, three-dimensional representation of a component with sub-grain scale resolution.

5.3.2 HR-EBSD

As discussed previously, a significant amount of work is being done to improve the amount of data that can be obtained from EBSD. Researchers are also working on developing higher quality and richer EBSD data sets. Conventional EBSD is designed to index many points in a short amount of time. As a consequence, the accuracy of orientations is often sacrificed through tradeoffs in variables such as binning parameters and processing time. These compromises result in a typical angular resolution of ±1°. High-resolution electron backscatter diffraction (HR-EBSD) employs saving and offline post-processing of the raw Kikuchi patterns to obtain far greater orientational accuracy around 0.1° [189, 190]. This improved accuracy allows more information to be extracted from EBSD data sets such as local measurements of stress and local geometrically necessary dislocation content. As one example of the use of such data, HR-EBSD has been used to measure geometrically necessary dislocations to investigate the interactions between dislocation networks and grain boundaries.

Because each pixel of information in conventional EBSD scans requires an entire image of Kikuchi bands to be saved in HR-EBSD [191], the data size increases by six orders of magnitude, which is literally one million times as much data! When HR-EBSD is combined with serial sectioning and/or faster speeds (typically, it was limited to ~2 patterns per second, but now ~1000 patterns per second), the data requirements will

increase even faster. Data management and analysis techniques will need to adapt to make use of these rich data sets.

5.3.3 TKD and PED

While HR-EBSD improves the angular resolution of EBSD, the technique is still limited to a spatial resolution of around 50 nm. This resolution is quite small for determining microtexture, but it becomes limited when analyzing small features such as grain boundary details, cell block boundaries, nanostructured materials [192] and void initiation in ductile metals [193]. Two techniques have been developed to improve the spatial resolution possible for Automated Crystal Orientation Mapping (ACOM): Transmission Kikuchi Diffraction (TKD) and Precession Electron Diffraction (PED). TKD [194] can provide improved resolution below 10 nm for closer examination of thin foil samples in a modified SEM-based technique similar to EBSD. This technique utilizes the forward scattered Kikuchi diffraction patterns. In contrast, PED utilizes an angular precessed electron beam in a STEM or TEM to produce a virtually kinematic diffraction pattern. [195] The resolution of PED is determined as the spot size of the instrument and can approach one nanometer. This technique has been utilized to create nanoscale resolution strain maps [196]. Both TKD and PED require rapid data and thorough analysis to create ACOM patterns and would greatly benefit from advancements in data handling and processing algorithms. These improvements can include the development of processes to enhance resolution and throughput by decreasing "fly-back errors" and other artifacts. Additionally, the methodologies discussed in section 2, as well as providing in-line data processing are areas in which the technology is advancing.

5.4 X-ray techniques

X-Ray Computed Tomography (XCT) is another area of microscopy that is dramatically increasing in usage as higher resolution techniques (nano-XCT) become commonplace. XCT has historically been used for non-destructive inspection of components. However, with the advent of additional techniques, its use as a research tool is increasing. Synchrotron radiation provides powerful capabilities for X-ray techniques including

improved resolution, fast testing times, and the power to go through thicker materials. Still, considerable progress has been made in lab-based XCT systems to allow easier access to “synchrotron” capabilities, albeit on a more limited scale. The relatively powerful lab-based XCT systems, with resolutions approaching one micron, are proving useful in analyzing flaws in additively manufactured metals among numerous other applications. Grain orientations can be measured through samples containing ~1000 grains [197] in a synchrotron. Even lab-based XCT systems are now incorporating Diffraction Contrast Tomography (DCT) systems to make similar measurements on a more limited scale.

As an analog to DIC on microscopy images, XCT data sets have the ability to perform three-dimensional measurements of strain using Digital Volume Correlation (DVC) [198, 199]. Like DIC, the DVC technique requires a speckle pattern. Creating three-dimensional speckle patterns are more challenging because they require embedding particles inside of the material to be studied. Often this results in a change in the bulk material properties, but trends can still be established. A few materials include an inherent three-dimensional speckle pattern, thereby allowing DVC to be performed directly on the material of interest [200]. DVC can help identify flaws in material and in-situ experiments can identify damage mechanisms. Furthermore, due to its sub-voxel resolution, DVC can often indicate where damage is accumulating before the user can visually detect damage.

In measuring orientations, EBSD is overtaking X-ray diffraction (XRD) as the dominant texture-characterization technique due to its superior resolution, but XRD is still quite valuable in a number of circumstances. XRD can be fast, does not require specimen polishing, and can performed under a less constrained range of conditions since it is not limited to surface applications within an SEM. Another powerful method for measuring orientations is neutron diffraction. Although the number of facilities is limited, this technique can provide grain orientation measurements in large volumes of material. All of these techniques are frequently combined with in situ loading and heating capabilities [201].

6. Potential Future Directions

The intersection of advanced electron microscopy and multi-scale modeling has greatly benefitted from the recent advancements in large data storage and processing over the last decade and are well suited to continue the same rapid growth rate over the next decade. The incorporation of Abberation Corrected (S)TEM (AC-(S)TEM), Energy-Filtered TEM (EF-TEM), Electron Tomography, Electron Holography, multi-beam SEM, orientation mapping, and DIC into the average electron microscopist toolbox is a testament to the advancements in large data processing that have occurred already. Similarly, the recent advancement in both electron diffraction patterns generated from MD simulations [112, 115] and the simulation of electron micrographs from strain maps [202, 203] indicates the growing coupling between multi-scale modeling and electron microscopy. In this section, we will discuss the potential opportunity to further the advancement of: 1) electron microscopy techniques, 2) validation and refinement of multi-scale modeling techniques, and 3) the direct coupling of electron microscopy and modeling efforts.

6.1. Future Directions of Electron Microscopy Techniques

The advancement in data collection, management, and interpretation can be directly tied to almost all advancements seen in the electron microscopy field over the last two decades. This is most drastically seen is the exponential increase in the amount of data collected as electron micrographs have evolved from images taken on film through the inclusion of CCD cameras to the recent commercialization of CMOS based direct electron detection cameras. This exponential increase in data collected has not only increased the amount of sample area imaged, but also greatly advanced in-situ electron microscopy, electron tomography, electron holography, and aberration correction. The corrections that made advances such as advanced aberration corrected, energy filtered, and to lesser extent electron tomography systems possible have been taken a step further in that the images collected during alignment are input into an automated or semi-automated script that cycles through the alignment parameters and the images collected until the desired alignments are complete. It is likely that this trend toward increasing automation of

alignments and related set-up procedure will continue to expand across the full range of advanced microscopy operational modes, continuing to increase the ease of use of these techniques for a broader set of experimental practitioners.

Utilizing advanced image recognition software and machine learning algorithms, it should be possible for more precise and accurate imaging conditions (such as direct control of the deviation parameter) to be achieved by an algorithm than by even the most well trained microscopist. This advance would provide the opportunity for the full set of imaging condition parameters (e.g., lens settings, tilts, temperature, vacuum conditions, etc.) to be optimized and recorded for these self-aligning and imaging microscopes. Such data would allow a much simpler interpretation of the data collected by a trained microscopist at the time, and would allow the direct input of data into future models (see sections 5.2 and 5.3). By collecting the metadata of imaging parameters with every image collected, data linkages and analysis should become easier and more thorough. To further extend this concept, this should be considered an iterative process and not a one directional operation. If any imaging conditions changes due to sample drift, a controlled in-situ stressor, or the like, then the microscope could be preprogramed to readjust at a given iteration rate and take images at set sample conditions or time intervals.

We expect that these advancements in automation will significantly advance the characterization of defect structures in the electron microscopy community in three ways. 1) The increased in resolution, stability, throughput, etc. will permit the development of new and refined techniques. Some of which are not currently imagined by the community. 2) The refinement, optimization, and increased ease of use of current advanced techniques will permit the application of these techniques to a broader and more challenging material set. 3) Due to similar improvements in refinement, optimization, miniaturization, and increased ease of use, the number of advanced techniques that can be done simultaneously or in close succession will increase. These three routes of advancement all require advances in large data processing and handling will provide a faster and more thorough understanding of our material world.

6.2. Future Directions of Modeling Validation and Refinement

One of the most difficult tasks in validating or refining an advanced model at any length scale is finding well pedigreed experimental data with which to compare. This challenge is typically overcome through close collaborations between theorist and experimentalist throughout the course of a project to ensure that new experimental data being created that informs the modeling effort. This approach often ignores the wealth of experimental data in the literature because a subset of the necessary model parameters or outputs for comparison are absent in the published manuscript. In the future, we anticipate increased utilization of global interconnectivity and cloud storage, enabling complete raw data sets and associated meta-data, such as from the experiments described in section 5.1, to be stored and reanalyzed by future researchers, achieving much greater potential for mining the wealth of experimental data collected across the community. Efforts along this direction have been initiated for hosting raw data or supplementary information on web-based hosting services like GitHuB. The access to raw data has permitted the reanalysis of data produced previously utilizing recent advancements in analytical software. The system we envision is the equivalent of a Google of Materials that is easy to access, provides access to the original raw data and the associated interpretation, and incorporates the material structure, property, and performance information over a range of conditions. This globally accessible repository of materials data can be easily used to guide, refine, and validate the development of predictive models at multiple length scales. Several academic, non-profit, and corporations are actively developing aspects of such a vision currently. If successful, this combination of data analytics, machine learning, database-driven approaches in modeling will not only benefit the theorist attempting to refine the models, but the experimentalist trying to determine where her data fits in the history of the associated research.

6.3. Future Directions towards Coupling Electron Microscopy and Modeling

The predicted big data impact on the advancement of electron microscopy and model validation alone are impactful; however, we believe that the greatest impact may come

from the direct, real time coupling of the two fields. If relevant models could run during an electron microscopy session, then the model could inform the choice of experimental parameters and interpretation in real time. The concept being that if a relevant model could be started utilizing the initial geometry, crystal orientation, and chemistry collected from the initial observation of the sample, then the model could be run in parallel to any in-situ SEM, TEM, or STEM experiment. This Parallel Experimenting would provide real time feedback between the model and the experimenting permitting both to be refined and developed during the simultaneous experiment/model effort. One can envision this effort being coupled both experimentally (OM, X-ray, SEM, dual-beam FIB to the TEM, etc.) and computationally (FEM, Mesoscale, MD, DFT) over multiple scales with key real-time observation made at the appropriate length and time scales. Such an effort has been proposed and is in early stages with the group led by Jones et al. [179].

Despite state-of-the-art computational models and experimental techniques, the current capabilities to characterize materials' structural defects are still limited by the extremely large dimensional spaces of potential interest and incomplete and uncertain information on available experimental and computational data. In particular, applying such advanced techniques is typically extremely time consuming and computationally expensive, limiting the possibility to conduct full analyses in the engineering-scale domain. To be applicable in engineering-scale components, many studies focus on a specific process or mechanism in a representative volume element (RVE), the smallest volume that would represent the homogenized behavior of the polycrystals. These techniques, along with practical capabilities in handling and integration of big data, will require ongoing development to realize the full potential of combining experimental microscopy and advanced modeling of structural defects. We expect rapid and sustained growth in the coupled modeling and electron microscopy characterization of defect structures as big data processing and handling is further developed.

Acknowledgments

Sandia National Laboratories is a multi-mission laboratory managed and operated by National Technology and Engineering Solutions of Sandia, LLC., a wholly owned subsidiary of Honeywell International, Inc., for the U.S. Department of Energy's National Nuclear Security Administration under contract DE-NA0003525.

This paper describes objective technical results and analysis. Any subjective views or opinions that might be expressed in the paper do not necessarily represent the views of the U.S. Department of Energy or the United States Government.

7. References

1. McDowell, D.L., A perspective on trends in multiscale plasticity. International Journal of Plasticity, 2010. 26(9): p. 1280-1309.
2. Kalinin, S.V., B.G. Sumpter, and R.K. Archibald, Big–deep–smart data in imaging for guiding materials design. Nature Materials, 2015. 14(10): p. 973-980.
3. Weinberger, C.R. and G.J. Tucker, Multiscale Materials Modeling for Nanomechanics. Springer Series in Materials Science. 2016: Springer International Publishing.
4. Canovic, S., et al., TEM and DFT investigation of CVD TiN/κ–Al2O3 multilayer coatings. Surface and Coatings Technology, 2007. 202(3): p. 522-531.
5. Halvarsson, M., A. Larsson, and S. Ruppi, Study of the interfacial structure and chemistry of CVD k-Al2O 3/TiC multilayer coatings. Micron, 2001. 32: p. 807-815.
6. Su, D.S., et al., Surface chemistry of Ag particles: identification of oxide species by aberration-corrected TEM and by DFT calculations. Angew Chem Int Ed Engl, 2008. 47(27): p. 5005-8.
7. Zasada, F., et al., Surface Structure and Morphology of M[CoM′]O4 (M = Mg, Zn, Fe, Co and M′ = Ni, Al, Mn, Co) Spinel Nanocrystals—DFT+U and TEM Screening Investigations. The Journal of Physical Chemistry C, 2014. 118(33): p. 19085-19097.

8. Avanesian, T., et al., Quantitative and Atomic-Scale View of CO-Induced Pt Nanoparticle Surface Reconstruction at Saturation Coverage via DFT Calculations Coupled with in Situ TEM and IR. J Am Chem Soc, 2017. 139(12): p. 4551-4558.
9. Miao, J., et al., Molecular dynamics simulations and morphology analysis of TEM imaged PVDF nanofibers. Polymer, 2017. 125: p. 190-199.
10. Pozuelo, M., et al., Nanotwins in nanocrystalline Mg–Al alloys: an insight from high-resolution TEM and molecular dynamics simulation. Philosophical Magazine Letters, 2013. 93(11): p. 640-647.
11. Tang, D.M., et al., Mechanical properties of bamboo-like boron nitride nanotubes by in situ TEM and MD simulations Strengthening effect. ACS NANO, 2011. 5(9): p. 7362-7368.
12. Schaeublin, R., et al., Correlating TEM images of damage in irradiated materials to molecular dynamics simulations. Journal of Nuclear Materials, 2002. 307-311: p. 98-992.
13. Eftink, B.P., et al., Deformation response of AgCu interfaces investigated by in situ and ex situ TEM straining and MD simulations. Acta Materialia, 2017. 138: p. 212-223.
14. Buehler, M., Atomistic Modeling of Materials Failure
. 2008: Springer US
.
15. Gao, K.W., L.J. Qiao, and W.Y. Chu, Molecular dynamics simulation andin situTEM study of crack healing. Materials Science and Technology, 2013. 18(10): p. 1109-1114.
16. Shekhawat, S.K., et al., Orientation-dependent plastic deformation in transformer steel: Experiments and dislocation dynamics simulations. Acta Materialia, 2015. 84: p. 256-264.
17. Dmitrieva, O., et al., Investigation of the internal substructure of microbands in a deformed copper single crystal: experiments and dislocation dynamics simulation. Modelling and Simulation in Materials Science and Engineering, 2010. 18(8): p. 085011.
18. Haider, M., et al., Electron microscopy image enhanced. Nature, 1998. 392: p. 768-769.

19. Dellby, N., et al., Progress in aberration-corrected scanning transmission electron microscopy. Journal of Electron Microscopy, 2001. 50(3): p. 177-185.
20. Batson, P.E., N. Dellby, and O.L. Krivanek, Sub-ångstrom resolution using aberration corrected electron optics. Nature, 2002. 418: p. 617-620.
21. Dahmen, U., et al., Background, status and future of the Transmission Electron Aberration-corrected Microscopy Project. Philosophical Transactions of the Royal Society A, 2009. 367: p. 3795-3808.
22. Findlay, S.D., et al., Robust atomic resolution imaging of light elements Applied Physics Letters, 2009. 95.
23. Haider, M., et al., A versatile, software configurable multichannel STEM detector for angle-resolved imaging. Ultramicroscopy, 1994. 54: p. 41-59.
24. Shibata, N., et al., New area detector for atomic-resolution scanning transmission electron microscopy. Journal of Electron Microscopy, 2010. 59(6): p. 473-479.
25. Battaglia, M., et al., A rad-hard CMOS active pixel sensor for electron microscopy. Nuclear Instruments and Methods in Physics Research A, 2009. 598: p. 642-649.
26. Tate, M.W., et al., High Dynamic Range Pixel Array Detector for Scanning Transmission Electron Microscopy. Microscopy and Microanalysis, 2016. 22: p. 237-249.
27. Miao, J., P. Ercius, and S.J.L. Billinge, Atomic electron tomography: 3D structures without crystals. Science, 2016. 353(6306): p. 1-8.
28. Williams, D.B. and C.B. Carter, Transmission Electron Microscopy: A Textbook for Materials Science (2nd edition). 2009: Springer.
29. Brydson, R., ed. Aberration-Corrected Analytical Transmission Electron Microscopy. 2011, RMS-Wiley.
30. Kirkland, E.J., Advanced Computing in Electron Microscopy. 2010: Springer.
31. Reimer, L., Transmission Electron Microscopy: Physics of Image Formation and Microanalysis, 2nd Edition. Springer Series in Optical Sciences, ed. P.W. Hawkes. Vol. 36. 1989, Berlin: Springer-Verlag.
32. Zhu, Y., et al., Interface lattice displacement measurement to 1 pm by geometric phase analysis on aberration-corrected HAADF STEM images. Acta Materialia, 2013. 61: p. 5646-5663.

33. Braidy, N., et al., Correcting scanning instabilities from images of periodic structures. Ultramicroscopy, 2012. 118: p. 67-76.
34. Jones, L. and P.D. Nellist, Identifying and Correcting Scan Noise and Drift in the Scanning Transmission Electron Microscope. Microscopy and Microanalysis, 2013. 19: p. 1050-1060.
35. Sang, X. and J.M. LeBeau, Revolving scanning transmission electron microscopy: correcting sample drift distortion without prior knowledge. Ultramicroscopy, 2014. 138: p. 28-35.
36. Binev, P., et al., High-Quality Image Formation by Nonlocal Means Applied to High-Angle Annular Dark-Field Scanning Transmission Electron Microscopy (HAADF-STEM), in Modelin Nanoscale Imaging in Electron Microscopy, T. Vogt, W. Dahmen, and P. Binev, Editors. 2012, Springer Science+Business Media: New York, Dordrecht, Heidelberg, London. p. 127-145.
37. Sang, X., et al., Precistion controlled atomic resolution scanning transmission electron microscopy using spiral scan pathways. Scientific Reports, 2017. 7: p. 1-11.
38. Binev, P., et al., Compressed Sensing and Electron Microscopy, in Modeling Nanoscale Imaging in Electron Microscopy, W.D. T. Vogt, P. Binev, Editor. 2012, Springer Science+Business Media: New York, Dordrecht, Heidelberg, London. p. 73-126.
39. Stevens, A., et al., The potential for Bayesian compressive sensing to significantly reduce electron dose in high-resolution STEM images. Microscopy, 2014. 63(1): p. 41-51.
40. Kovarik, L., et al., Implementing an accurate and rapid sparse sampling approach for low-dose atomic resolution STEM imaging. Applied Physics Letters, 2016. 109.
41. Béché, A., et al., Development of a fast electromagnetic beam blanker for compressed sensing in scanning transmission electron microscopy. Applied Physics Letters, 2016. 108: p. 1-5.
42. Hwang, S., et al., Towards the low-dose characterization of beam sensitive nanostructures via implementation of sparse image acquisition in scanning transmission electron microscopy. Measurement Science and Technology, 2017. 28: p. 1-9.

43. Dahmen, U., et al., Atomic structure of a Sigma 99 grain boundary in aluminium: a comparison between atomic-resolution observation and pair potential and embedded-atom simulations. Philosophical Magazine Letters, 1990. 62(5): p. 327-335.
44. Mills, M.J., et al., High resolution transmission electron microscopy of grain boundaries in aluminum and correlation with atomistic calculations. Ultramicroscopy, 1992. 40: p. 247-257.
45. Medlin, D.L., et al., HRTEM Observations of a Σ=3 {112} Bicrystal boundary in Aluminum, in Atomic-Scale Imaging of Surfaces and Interfaces, D.K. Biegelsen, D.J. Smith, and S.Y. Tong, Editors. 1992, Materials Research Society. p. 91-96.
46. Campbell, G.H., et al., Atomic Structure of the (310) twin in niobium: Experimental Determination and Comparison with Experimental Predictions. Physical Review Letters, 1993. 70(4): p. 449-452.
47. Medlin, D.L., et al., Structure of the (0001) basal twin boundary in Bi2Te3. Journal of Applied Physics, 2010. 108: p. 1-6.
48. Medlin, D.L., et al., Defect character at grain boundary facet junctions: Analysis of an asymmetric ∑=5 grain boundary in Fe. Acta Materialia, 2017. 124: p. 383-396.
49. Ernst, F., et al., Theoretical Prediction and Direct Observation of the 9R structure in Ag. Physical Review Letters, 1992. 69(4): p. 620-623.
50. Wolf, U., et al., The influence of grain boundary inclination on the structure and energy of Σ=3 grain boundaries in copper. Philosophical Magazine A, 1992. 66(6): p. 991-1016.
51. Rittner, J.D., D.N. Seidman, and K.L. Merkle, Grain boundary dissociation by the emission of stacking faults. Physical Review B, 1996. 53(8): p. R4241-R4244.
52. Medlin, D.L., S.M. Foiles, and D. Cohen, A Dislocation-Based Description of Grain Boundary Dissociation: Application to a 90 Degree <110> Tilt Boundary in Gold. Acta materialia, 2001. 49(18): p. 3687-3695.
53. Lucadamo, G. and D.L. Medlin, Geometric Origin of Hexagonal Close Packing at a Grain Boundary in Gold. Science, 2003. 300: p. 1272-1275.
54. Medlin, D.L. and J.C. Hamilton, Formation of Hexagonal Close Packing at a Grain Boundary in Gold by the Dissociation of a Dense Array of Crystal Lattice Dislocations. Journal of Materials Science, 2009. 44: p. 3608-3617.

55. Medlin, D.L., et al., Climb and Glide of a/3<111> Dislocations in an Aluminum S=3 Boundary. Philosophical Magazine A, 1997. 75(3): p. 733-747.
56. Foiles, S.M. and D.L. Medlin, Structure and Climb of 1/3<111> Twin Dislocations in Aluminum. Materials Science and Engineering A, 2001. 319-321: p. 102-106.
57. Marquis, E.A. and D.L. Medlin, Structural duality of 1/3<111> twin-boundary disconnections. Philosophical Magazine Letters, 2005. 85(8): p. 387-394.
58. Kovarik, L., et al., Microtwinning and other shearing mechanisms at intermediate temperatures in Ni-based superalloys. Progress in Materials Science, 2009. 54: p. 839-873.
59. Marquis, E.A., et al., Finite Size Effects on the Structure of Grain Boundaries. Physical Review Letters, 2004. 93: p. 156101.
60. Mendelev, M.I., et al., Development of new interatomic potentials appropriate for crystalline and liquid iron. Philosophical Magazine, 2003. 83(35): p. 3977-3994.
61. Bierwolf, R., et al., Direct measurement of local lattice distortions in strained layer structures by HREM. Ultramicroscopy, 1993. 49: p. 273-285.
62. Marks, L.D., Wiener-filter enhancement of noisy HREM images. Ultramicroscopy, 1996. 62: p. 43-52.
63. Kilaas, R., Optimal and near-optimal filters in high-resolution electron microscopy. Journal of Microscopy, 1998. 190: p. 45-51.
64. Hofmann, D. and F. Ernst, Quantitative high-resolution transmission electron miroscopy of the incoherent ∑3(211) boundary in Cu. Ultramicroscopy, 1994. 53: p. 205-221.
65. Paciornik, S., et al., A pattern recognition technique for the analysis of grain boundary structure by HREM. Ultramicroscopy, 1996. 62: p. 15-27.
66. Bayle, P., et al., Quantitative analysis of the deformation and chemical profiles of strained multilayers. Ultramicroscopy, 1994. 56: p. 94-107.
67. Jouneau, P.H., et al., Strain mapping of ultrathin epitaxial ZnTe and MnTe layers embedded in CdTe. J. Appl. Phys., 1994. 75(11): p. 7310-7316.
68. Barthel, J. Dr. Probe - High-resolution (S)TEM image simulation software. 2017 [cited 2017 December 29, 2017]; Available from: http://www.er-c.org/barthel/drprobe/.

69. Stadelmann, P. JEMS-SAAS. 2017 [cited 2017 December 29, 2017]; Available from: http://www.jems-saas.ch/.
70. Koch, C., Determination of Core Structure Periodicity and Point Defect Density along Dislocations. 2002, Arizona State University.
71. Koch, C. QSTEM: Quantitative TEM/STEM Simulations. 2017 [cited 2017 December 29. 2017]; Available from: https://www.physics.hu-berlin.de/en/sem/software/software_qstem.
72. Kirkland, E.J. computem: Transmission Electron Microscope Image Simulation. 2017 [cited 2017 December 29, 2017]; Available from: https://sourceforge.net/projects/computem/.
73. King, W.E., et al., Quantitative HREM observations of the ∑11(113)/[-110] grain-boundary structure in aluminium and comparison with atomistic simulation. Journal of Microscopy, 1998. 190: p. 131-143.
74. Möbus, G., et al., Iterative structure retrieval techniques in HREM: a comparative study and modular program package. Journal of Microscopy, 1998. 190: p. 109-130.
75. Möbus, G. and O. Kienzle, Probability calculus for quantitative HREM. Part I: Monte-Carlo and point cloud techniques. Ultramicroscopy, 2000. 85: p. 183-198.
76. Möbus, G., Probability calculus for quantitative HREM. Part II: Entropy and likelihood concepts. Ultramicroscopy, 2000. 85: p. 199-213.
77. Dekkar, A.J.d., et al., Maximum likelihood estimation of structure parameters from high resolution electron microscopy images. Part I: A theoretical framework. Ultramicroscopy, 2005. 104: p. 83-106.
78. Aert, S.V., et al., Maximum likelihood estimation of structure parameters from high resolution electron microscopy images. Part II: A practical example. Ultramicroscopy, 2005. 104: p. 107-125.
79. Kelchner, C.L., S.J. Plimpton, and J.C. Hamilton, Dislocation nucleation and defect structure during surface indentation. Physical Review B, 1998. 58(17): p. 11085-11088.
80. Medlin, D.L., J.C. Hamilton, and O. Uche, Analysis of Dissociated Grain Boundary Structure: Application of the Local Centrosymmetry Parameter to HRTEM Images. Microscopy and Microanalysis, 2007. 13(Supplement 2).

81. Vorontsov, V.A., et al., High-resolution electron microscopy of dislocation ribbons in a CMSX-4 superalloy single crystal. Acta Materialia, 2012: p. 4866-4878.
82. Muntifering, B., et al., Intra-variant substructure in Ni-Mn-Ga martensite: Conjugation boundaries. Acta Materialia, 2014. 71: p. 255-263.
83. Hartley, C.S. and Y. Mishin, Characterization and visualization of the lattice misfit associated with dislocation cores. Acta Materialia, 2005. 53: p. 1313-1321.
84. Mendis, B.G., et al., Use of the Nye tensor in analyzing HREM images of bcc screw dislocations. Philosophical Magazine, 2006. 86(29-31): p. 4607-4640.
85. Smith, T.M., et al., Atomic-scale characterization and modeling of 60° dislocations in a high-entropy alloy. Acta Materialia, 2016. 110: p. 352-363.
86. Benthem, K.v., et al., Three-dimensional imaging of individual hafnium atoms inside a semiconductor device. Applied Physics Letters, 2005. 87: p. 1-3.
87. Behan, G., et al., Three-Dimensional Imaging by Optical Sectioning in the Aberration-Corrected Scanning Transmission Electron Microscope. Philosophical Transactions of the Royal Society A, 2009. 367: p. 3825-3844.
88. Lozano, J.G., et al., Direct Observation of Depth-Dependent Atomic Displacements Associated with Dislocations in Gallium Nitride. Physical Review Letters, 2014. 113: p. 1-5.
89. Yang, H., et al., Imaging screw dislocations at atomic resolution by aberration-corrected electron optical sectioning. Nature Communications, 2015: p. 1-7.
90. Aert, S.V., et al., Three-dimensional atomic imaging of crystalline nanoparticles. Nature, 2011. 470: p. 374-377.
91. Goris, B., et al., Atomic-scale determination of surface facets in gold nanorods. Nature Materials, 2012. 11: p. 930-935.
92. Scott, M.C., et al., Electron tomography at 2.4-ångstrom resolution. Nature, 2012. 483: p. 444-447.
93. Chen, C.-C., et al., Three-dimensional imaging of dislocations in a nanoparticle at atomic resolution. Nature, 2013. 496: p. 74-77.
94. Goris, B., et al., Measuring Lattice Strain in Three Dimensions though Electron Microscopy. Nano Letters, 2015. 15: p. 6996-7001.

95. Xu, R., et al., Three-dimensional coordinates of individual atoms in materials revealed by electron tomography. Nature Materials, 2015. 14: p. 1099-1103.
96. Hÿtch, M.J., E. Snoeck, and R. Kilaas, Quantitative measurement of displacement and strain fields from HREM micrographs. Ultramicroscopy, 1998. 74: p. 131-146.
97. Johnson, C.L., et al., Effects of elastic anisotropy on strain distributions in decahedral gold nanoparticles. Nature Materials, 2008. 7: p. 120-124.
98. Catalan, G., et al., Flexoelectric rotation of polarization in ferroelectric thin films. Nature Materials, 2011. 10: p. 963-967.
99. Gao, P., et al., Atomic-scale mechanisms of ferroelastic domain-wall-mediated ferroelectric switching. Nature Communications, 2013. 4(2791): p. 1-9.
100. Hÿtch, M.J., J.-L. Putaux, and J. Thibault, Stress and strain around grain-boundary dislocations measured by high-resolution electron microscopy. Philosophical Magazine, 2008. 86(29-31): p. 4641-4656.
101. Azizi, A., et al., Dislocation motion and grain boundary migration in two-dimensional tungsten disuphide. Nature Communications, 2014. 5(4867): p. 1-7.
102. Johnson, C.L., M.J. Hÿtch, and P.R. Buseck, Nanoscale waviness of low-angle grain boundaries. PNAS, 2004. 101(52): p. 17936-17939.
103. Biswas, K., et al., High-performance bulk thermoelectrics with all-scale hierarchical architectures. Nature, 2012. 489: p. 414-418.
104. Bonell, F., et al., Influence of misfit dislocations on the magnetoresistance of MgO-based epitaxial magnetic tunnel junctions. Physical Review B, 2010. 82(092405): p. 1-4.
105. Chu, M.-W., et al., Impact of misfit dislocations on the polarization instability of epitaxial nanostructured ferroelectric perovskites. Nature Materials, 2004. 3: p. 87-90.
106. Chu, M.-W., et al., Elastic coupling between 90° twin walls and interfacial dislocations in epitaxial ferrolectric perovskites: A quantitative high-resolution transmission electron microscopy study. Physical Review B, 2005. 72(174112): p. 1-5.
107. Mata, M.d.l., et al., Atomic Scale Strain Relaxation in Axial Semiconductor III-V Nanowire Heterostructures. Nano Letters, 2014. 14: p. 6614-6620.
108. He, J., et al., Microstructure-Lattice ThermalConductivity Correlation in Nanostructured PgTe0.7S0.3 Thermoelectric Materials. Advanced Functional Materials, 2010. 20: p. 764-772.

109. Hÿtch, H.J., J.-L. Putaux, and J.-M. Pénisson, Measurement of the displacement field of dislocations to 0.03Å by electron microscopy. Nature, 2003. 423: p. 270-273.
110. Peters, J.J.P., et al., Artefacts in geometric phase analysis of compound materials. Ultramicroscopy, 2015. 157: p. 91-97.
111. Coleman, S., D. Spearot, and L. Capolungo, Virtual diffraction analysis of Ni [0 1 0] symmetric tilt grain boundaries. Modelling and Simulation in Materials Science and Engineering, 2013. 21(5): p. 055020.
112. Coleman, S.P. and D.E. Spearot, Atomistic simulation and virtual diffraction characterization of homophase and heterophase alumina interfaces. Acta Materialia, 2015. 82: p. 403-413.
113. Plimpton, S., P. Crozier, and A. Thompson, LAMMPS-large-scale atomic/molecular massively parallel simulator. Sandia National Laboratories, 2007. 18: p. 43-43.
114. Stadelmann, P., EMS-a software package for electron diffraction analysis and HREM image simulation in materials science. Ultramicroscopy, 1987. 21(2): p. 131-145.
115. Coleman, S.P., M.M. Sichani, and D.E. Spearot, A computational algorithm to produce virtual x-ray and electron diffraction patterns from atomistic simulations. Jom, 2014. 66(3): p. 408-416.
116. Ruska, E., The development of the electron-microscope and of electron-microscopy, Reviews of Modern Physics, 1987. 59(3): p. 627-638.
117. Jenkins, M.L. and M.A. Kirk, Characterisation of radiation damage by transmission electron microscopy. 2000: CRC Press, Taylor & Francis Group, FL, USA.
118. Kirk, M., X. Yi, and M. Jenkins, Characterization of irradiation defect structures and densities by transmission electron microscopy. Journal of Materials Research, 2015. 30(9): p. 1195-1201.
119. Yi, X., et al., In situ study of self-ion irradiation damage in W and W–5Re at 500° C. Philosophical Magazine, 2013. 93(14): p. 1715-1738.
120. Yi, X., et al., Characterisation of radiation damage in W and W-based alloys from 2MeV self-ion near-bulk implantations. Acta Materialia, 2015. 92: p. 163-177.
121. Hardy, G.J. and M.L. Jenkins, EVIDENCE FOR STACKING-FAULT TETRAHEDRA FORMED FROM SELF-INTERSTITIALS IN ELECTRON-IRRADIATED

SILVER. Philosophical Magazine a-Physics of Condensed Matter Structure Defects and Mechanical Properties, 1985. 52(2): p. L19-L23.
122. Sigle, W., M.L. Jenkins, and J.L. Hutchison, DETERMINATION OF THE NATURE OF STACKING-FAULT TETRAHEDRA IN ELECTRON-IRRADIATED SILVER BY HIGH-RESOLUTION STRUCTURAL IMAGING. Philosophical Magazine Letters, 1988. 57(5): p. 267-271.
123. Arganda-Carreras, I., et al., Trainable Weka Segmentation: a machine learning tool for microscopy pixel classification. Bioinformatics, 2017. 33(15): p. 2424-2426.
124. Sorzano, C., et al., Automatic particle selection from electron micrographs using machine learning techniques. Journal of structural biology, 2009. 167(3): p. 252-260.
125. Kusne, A.G., et al., On-the-fly machine-learning for high-throughput experiments: search for rare-earth-free permanent magnets. Scientific reports, 2014. 4: p. 6367.
126. Marian, J., et al., Recent advances in modeling and simulation of the exposure and response of tungsten to fusion energy conditions. Nuclear Fusion, 2017. 57(9): p. 092008.
127. De Graef, M., Introduction to conventional transmission electron microscopy. 2003: Cambridge University Press.
128. Venkatakrishnan, S.V., et al. Model based iterative reconstruction for bright field electron tomography. in Computational Imaging XI. 2013. International Society for Optics and Photonics.
129. Venkatakrishnan, S.V., et al., A model based iterative reconstruction algorithm for high angle annular dark field-scanning transmission electron microscope (HAADF-STEM) tomography. IEEE Transactions on Image Processing, 2013. 22(11): p. 4532-4544.
130. Ribis, J., et al., Radiation-induced cavities in aluminium alloy imaged by in line electron holography. Philosophical Magazine, 2016. 96(24): p. 2504-2517.
131. Frank, J., Electron tomography. 1992: Springer Science - Business Media New York, USA.
132. Vanhecke, D., et al., Cryo-electron tomography: methodology, developments and biological applications. Journal of microscopy, 2011. 242(3): p. 221-227.
133. Li, M., et al., Study of defect evolution by TEM with in situ ion irradiation and coordinated modeling. Philosophical Magazine, 2012. 92(16): p. 2048-2078.

134. Xu, D., et al., Defect microstructural evolution in ion irradiated metallic nanofoils: Kinetic Monte Carlo simulation versus cluster dynamics modeling and in situ transmission electron microscopy experiments. Applied Physics Letters, 2012. 101(10): p. 101905.
135. Xu, D., et al., Recent work towards understanding defect evolution in thin molybdenum foils through in situ ion irradiation under TEM and coordinated cluster dynamics modeling. Current Opinion in Solid State and Materials Science, 2012. 16(3): p. 109-114.
136. Faruqi, A. and R. Henderson, Electronic detectors for electron microscopy. Current opinion in structural biology, 2007. 17(5): p. 549-555.
137. Prydderch, M., et al., A 512× 512 CMOS monolithic active pixel sensor with integrated ADCs for space science. Nuclear Instruments and Methods in Physics Research Section A: Accelerators, Spectrometers, Detectors and Associated Equipment, 2003. 512(1-2): p. 358-367.
138. Evans, D., et al., CMOS active pixel sensors for ionising radiation. Nuclear Instruments and Methods in Physics Research Section A: Accelerators, Spectrometers, Detectors and Associated Equipment, 2005. 546(1-2): p. 281-285.
139. Turchetta, R., et al., CMOS Monolithic Active Pixel Sensors (MAPS): New 'eyes' for science. Nuclear Instruments and Methods in Physics Research Section A: Accelerators, Spectrometers, Detectors and Associated Equipment, 2006. 560(1): p. 139-142.
140. McMullan, G., et al., Detective quantum efficiency of electron area detectors in electron microscopy. Ultramicroscopy, 2009. 109(9): p. 1126-1143.
141. Ruskin, R.S., Z. Yu, and N. Grigorieff, Quantitative characterization of electron detectors for transmission electron microscopy. Journal of structural biology, 2013. 184(3): p. 385-393.
142. Stach, E.A., et al., Exploiting a direct detection camera for in-situ microscopy. Microcopy Microanal, 2013. 19: p. 392-393.
143. Li, X., et al., Electron counting and beam-induced motion correction enable near-atomic-resolution single-particle cryo-EM. Nature methods, 2013. 10(6): p. 584.
144. Zou, L., et al., In situ atomic-scale imaging of the metal/oxide interfacial transformation. Nature communications, 2017. 8(1): p. 307.

145. Stach, E., et al., Automated image acquisition and analysis of beam sensitive samples. Microscopy and Microanalysis, 2017. 23(S1): p. 1788-1789.
146. Gammer, C., et al., Strain Mapping during In-situ Deformation using a High-Speed Electron Detector. Microscopy and Microanalysis, 2015. 21: p. 2325.
147. Ozdol, V., et al., Strain mapping at nanometer resolution using advanced nano-beam electron diffraction. Applied Physics Letters, 2015. 106(25): p. 253107.
148. Gammer, C., et al., Local and transient nanoscale strain mapping during in situ deformation. Applied Physics Letters, 2016. 109(8): p. 081906.
149. Armstrong, M.R., et al., Practical considerations for high spatial and temporal resolution dynamic transmission electron microscopy. Ultramicroscopy, 2007. 107(4-5): p. 356-367.
150. LaGrange, T., et al., Single-shot dynamic transmission electron microscopy. Applied Physics Letters, 2006. 89(4).
151. LaGrange, T., et al., Nanosecond time-resolved investigations using the in situ of dynamic transmission electron microscope (DTEM). Ultramicroscopy, 2008. 108(11): p. 1441-1449.
152. Williamson, J.C., et al., Clocking transient chemical changes by ultrafast electron diffraction. Nature, 1997. 386(6621): p. 159.
153. Baum, P. and A.H. Zewail, Breaking resolution limits in ultrafast electron diffraction and microscopy. Proceedings of the National Academy of Sciences, 2006. 103(44): p. 16105-16110.
154. Zewail, A.H., 4D ultrafast electron diffraction, crystallography, and microscopy. Annu. Rev. Phys. Chem., 2006. 57: p. 65-103.
155. Feist, A., et al., Ultrafast transmission electron microscopy using a laser-driven field emitter: Femtosecond resolution with a high coherence electron beam. Ultramicroscopy, 2017. 176: p. 63-73.
156. Yang, D.-S., O.F. Mohammed, and A.H. Zewail, Scanning ultrafast electron microscopy. Proceedings of the National Academy of Sciences of the United States of America, 2010. 107(34): p. 14993-14998.

157. Yang, D.-S., O.F. Mohammed, and A.H. Zewail, Environmental Scanning Ultrafast Electron Microscopy: Structural Dynamics of Solvation at Interfaces. Angewandte Chemie-International Edition, 2013. 52(10): p. 2897-2901.
158. Carl Zeiss, I. MultiSEM 505/506, The World's Fastest Scanning Electron Microscopes. 2017 10/25/2017]; Available from: https://www.zeiss.com/microscopy/us/products/scanning-electron-microscopes/multisem.html.
159. Chu, T., W. Ranson, and M.A. Sutton, Applications of digital-image-correlation techniques to experimental mechanics. Experimental mechanics, 1985. 25(3): p. 232-244.
160. Dally, J.W. and W.F. Riley, Experimental Stress Analysis. 4th ed. 2005, Knoxville, TN: College House Enterprises, LLC.
161. Carroll, J., et al., An experimental methodology to relate local strain to microstructural texture. Review of Scientific Instruments, 2010. 81(8): p. 083703.
162. Kammers, A.D., et al., The effect of microstructure heterogeneity on the microscale deformation of ultrafine-grained aluminum. Journal of Materials Research, 2014. 29(15): p. 1664-1674.
163. Holm, E.A. and C.C. Battaile, The computer simulation of microstructural evolution. JOM, 2001. 53(9): p. 20-23.
164. Abdeljawad, F., et al., Connecting microstructural coarsening processes to electrochemical performance in solid oxide fuel cells: An integrated modeling approach. J. Power Sources, 2014. 250: p. 319-331.
165. Abdeljawad, F. and S.M. Foiles, Stabilization of Nanocrystalline Alloys via Grain Boundary Segregation: A Diffuse Interface Model. Acta Materialia, 2015. 250: p. 159-171.
166. Lim, H., et al., Incorporating physically-based microstructures in materials modeling: Bridging phase field and crystal plasticity frameworks. Modelling and Simulation in Materials Science and Engineering, 2016. 24(4): p. 045016.
167. Gruber, J., et al., Development of physically based atomistic microstructures: The effect on the mechanical response of polycrystals. Computational Materials Science, 2017. 128: p. 29-36.

168. Montes de Oca Zapiain, D., E. Popova, and S.R. Kalidindi, Prediction of microscale plastic strain rate fields in two-phase composites subjected to an arbitrary macroscale strain rate using the materials knowledge system framework. Acta Materialia, 2017. 141: p. 230-240.
169. Popova, E., et al., Process-Structure Linkages Using a Data Science Approach: Application to Simulated Additive Manufacturing Data. Integrating Materials and Manufacturing Innovation, 2017. 6(1): p. 54-68.
170. Alharbi, H.F. and S.R. Kalidindi, Crystal plasticity finite element simulations using a database of discrete Fourier transforms. International Journal of Plasticity, 2015. 66: p. 71-84.
171. Knezevic, M., H.F. Al-Harbi, and S.R. Kalidindi, Crystal plasticity simulations using discrete Fourier transforms. Acta Materialia, 2009. 57(6): p. 1777-1784.
172. Knezevic, M., S.R. Kalidindi, and D. Fullwood, Computationally efficient database and spectral interpolation for fully plastic Taylor-type crystal plasticity calculations of face-centered cubic polycrystals. International Journal of Plasticity, 2008. 24(7): p. 1264-1276.
173. Carroll, J.D., et al., On the interactions between strain accumulation, microstructure, and fatigue crack behavior. International Journal of Fracture, 2013. 180(2): p. 223-241.
174. Carroll, J., et al., Investigation of fatigue crack closure using multiscale image correlation experiments. Engineering Fracture Mechanics, 2009. 76(15): p. 2384-2398.
175. McNeill, S.R., W.H. Peters, and M.A. Sutton, Estimation of stress intensity factor by digital image correlation. Engineering Fracture Mechanics, 1987. 28(1): p. 101-112.
176. Krishnamoorthy, H. and H. Tippur, Extracting fracture parameters using local collocation of full-field displacement data. Experimental Techniques, 1998. 22(1): p. 22-25.
177. Sanford, R.J., Determining fracture parameters with full-field optical methods. Experimental Mechanics, 1989. 29(3): p. 241-247.
178. Grédiac, M., et al., The Virtual Fields Method for Extracting Constitutive Parameters From Full-Field Measurements: a Review. Strain, 2006. 42(4): p. 233-253.

179. Jones, E.M.C., et al., Parameter Covariance and Non-Uniqueness in Material Model Calibration using the Virtual Fields Method. Computational Materials Science, 2018, 152: p. 268 - 290.
180. Reu, P.L., A Study of the Influence of Calibration Uncertainty on the Global Uncertainty for Digital Image Correlation Using a Monte Carlo Approach. Experimental Mechanics, 2013. 53(9): p. 1661-1680.
181. Lim, H., et al., Grain-scale Experimental Validation of Crystal Plasticity Finite Element Simulations of Tantalum Oligocrystals. International Journal of Plasticity, 2014.
182. Carroll, J.D., et al., An experimental statistical analysis of stress projection factors in BCC tantalum. Materials Science and Engineering A, 2013. 581(0): p. 108-118.
183. Carroll, J.D., et al., High resolution digital image correlation measurements of strain accumulation in fatigue crack growth. International Journal of Fatigue, 2013. 57(0): p. 140-150.
184. Kammers, A.D. and S. Daly, Digital Image Correlation under Scanning Electron Microscopy: Methodology and Validation. Experimental Mechanics, 2013. 53(9): p. 1743-1761.
185. Lim, H., et al., Grain-scale experimental validation of crystal plasticity finite element simulations of tantalum oligocrystals. International Journal of Plasticity, 2014. 60: p. 1-18.
186. Frazier, W.E., Metal Additive Manufacturing: A Review. Journal of Materials Engineering and Performance, 2014. 23(6): p. 1917-1928.
187. Chen, Y., et al., Optimization of EBSD parameters for ultra-fast characterization. Journal of Microscopy, 2012. 245(2): p. 111-118.
188. Instruments, O. Symmetry EBSD Detector. 2018; Available from: https://www.oxford-instruments.com/OxfordInstruments/media/nanoanalysis/Symmetry/Symmetry-brochure-web.pdf.
189. Wilkinson, A.J., Measurement of elastic strains and small lattice rotations using electron back scatter diffraction. Ultramicroscopy, 1996. 62(4): p. 237-247.
190. Ruggles, T.J. and D.T. Fullwood, Estimations of bulk geometrically necessary dislocation density using high resolution EBSD. Ultramicroscopy, 2013. 133(0): p. 8-15.

191. Hansen, L.T., et al., Influence of Noise-Generating Factors on Cross-Correlation Electron Backscatter Diffraction (EBSD) Measurement of Geometrically Necessary Dislocations (GNDs). Microscopy and Microanalysis, 2017. 23(3): p. 460-471.
192. Trimby, P.W., Orientation mapping of nanostructured materials using transmission Kikuchi diffraction in the scanning electron microscope. Ultramicroscopy, 2012. 120: p. 16-24.
193. Noell, P., et al., Do voids nucleate at grain boundaries during ductile rupture? Acta Materialia, 2017. 137: p. 103-114.
194. Keller, R.R. and R.H. Geiss, Transmission EBSD from 10 nm domains in a scanning electron microscope. Journal of Microscopy, 2012. 245(3): p. 245-251.
195. Portillo, J., et al. Precession electron diffraction assisted orientation mapping in the transmission electron microscope. in Materials science forum. 2010. 644: p. 1-7.
196. Rouviere, J.-L., et al., Improved strain precision with high spatial resolution using nanobeam precession electron diffraction. Applied Physics Letters, 2013. 103(24): p. 241913.
197. Herbig, M., et al., 3-D growth of a short fatigue crack within a polycrystalline microstructure studied using combined diffraction and phase-contrast X-ray tomography. Acta Materialia, 2011. 59(2): p. 590-601.
198. Bay, B.K., et al., Digital volume correlation: Three-dimensional strain mapping using X-ray tomography. Experimental Mechanics, 1999. 39(3): p. 217-226.
199. Gates, M., J. Lambros, and M.T. Heath, Towards high performance digital volume correlation. Experimental Mechanics, 2011. 51(4): p. 491-507.
200. Croom, B.P., et al., Digital volume correlation with fragile speckle patterns: Evaluating strain localization in syntactic foams. (Submitted), 2018.
201. Brown, D.W., et al., In Situ Neutron Diffraction Study of the Influence of Microstructure on the Mechanical Response of Additively Manufactured 304L Stainless Steel. Metallurgical and Materials Transactions A, 2017. 48(12): p. 6055-6069.
202. Callahan, P.G., et al., 3D Texture Visualization Approaches: Theoretical Analysis and Examples, Journal of Applied Crystallography, 2017, 50 (2): p. 430-440.
203. Picard, Y.N., et al., Future prospects for defect and strain analysis in the SEM via electron channeling. Microscopy Today, 2012. 20(2): p. 12-16.

Acknowledgments

Sandia National Laboratories is a multi-mission laboratory managed and operated by National Technology and Engineering Solutions of Sandia, LLC., a wholly owned subsidiary of Honeywell International, Inc., for the U.S. Department of Energy's National Nuclear Security Administration under contract DE-NA0003525.

This paper describes objective technical results and analysis. Any subjective views or opinions that might be expressed in the paper do not necessarily represent the views of the U.S. Department of Energy or the United States Government.